

Ubiquity of Methanol and its related Chemical Segregation in Orion Starless Cores: the ALMASOP Sample

SHIH-YING HSU ¹, SHENG-YUAN LIU ¹, XUNCHUAN LIU ², PAK SHING LI ², KEN'ICHI TATEMATSU ^{3,4},
NAOMI HIRANO ¹, SHENG-JUN LIN ¹, KEE-TAE KIM ^{5,6}, SHANGHUO LI ^{7,8}, TIE LIU ² AND DIPEN SAHU ⁹

¹*Institute of Astronomy and Astrophysics, Academia Sinica, No.1, Sec. 4, Roosevelt Rd, Taipei 10617, Taiwan (R.O.C.)*

²*Shanghai Astronomical Observatory, Chinese Academy of Sciences, Shanghai 200030, PR China*

³*Nobeyama Radio Observatory, National Astronomical Observatory of Japan, National Institutes of Natural Sciences, 462-2 Nobeyama, Minamimaki, Minamisaku, Nagano 384-1305, Japan*

⁴*Astronomical Science Program, The Graduate University for Advanced Studies, SOKENDAI, 2-21-1 Osawa, Mitaka, Tokyo 181-8588, Japan*

⁵*Korea Astronomy and Space Science Institute (KASI), 776 Daedeokdae-ro, Yuseong-gu, Daejeon 34055, Republic of Korea*

⁶*University of Science and Technology, Korea (UST), 217 Gajeong-ro, Yuseong-gu, Daejeon 34113, Republic of Korea*

⁷*School of Astronomy and Space Science, Nanjing University, 163 Xianlin Avenue, Nanjing 210023, People's Republic of China*

⁸*Key Laboratory of Modern Astronomy and Astrophysics (Nanjing University), Ministry of Education, Nanjing 210023, People's Republic of China*

⁹*Physical Research laboratory, Navrangpura, Ahmedabad, Gujarat 380009, India*

(Accepted December 2, 2025)

Submitted to ApJ

ABSTRACT

Complex organic molecules (COMs) in starless cores provide critical insights into the early stages of star formation and prebiotic chemistry. We present a chemical survey of 16 starless cores (including five prestellar cores) in the Orion A and B molecular clouds, targeting CH₃OH, N₂H⁺, CCS, and c-C₃HD, using the Atacama Compact Array (ACA) and the Yebes 40-m telescope. CH₃OH was detected toward all targets, confirming its ubiquity in starless cores, consistent with previous surveys in Taurus and Perseus. ACA imaging shows that CH₃OH, CCS, and c-C₃HD generally trace the outer layers of the dense cores outlined by N₂H⁺, each exhibiting distinct spatial distributions. Meanwhile, Comparison with Yebes data reveals an extended, flattened CH₃OH component. CCS and c-C₃HD tend to be detected or non-detected together across cores, while cores near dust-rich regions on a large scale often lack both, suggesting environmental influences linked to the interstellar radiation field. Within individual cores, CCS typically resides in an outer layer relative to c-C₃HD. Our findings underscore the importance of high-resolution studies for understanding the origins and spatial differentiation of COMs and carbon-chain molecules in cold, quiescent environments.

Keywords: astrochemistry — ISM: molecules — stars: formation and low-mass

1. INTRODUCTION

Complex organic molecules (COMs) in star-forming regions are of great interest due to their potential link to prebiotic chemistry in emerging planetary systems. COMs, such as CH₃OH, are defined as saturated organic molecules composed of at least six atoms (Herbst & van Dishoeck

2009). While COMs have been extensively studied in protostellar cores (e.g., Belloche et al. 2020; Hsu et al. 2020; van Gelder et al. 2020; Yang et al. 2021; Hsu et al. 2022; Bouvier et al. 2022), their presence and behavior in starless cores remain less well studied. Under the common nomenclature, a starless core is a dense condensation of gas and dust within a molecular cloud that lacks any protostellar object. Meanwhile, prestellar cores are considered a subset of starless cores that are gravitationally bound and expected to evolve into protostellar cores in the future (e.g., Di Francesco et al. 2006). In this paper, we use the term

seansyhsu@gmail.com

syliu@asiaa.sinica.edu.tw

liuxunchuan001@gmail.com

“starless cores” in a broader sense which includes those identified as prestellar cores.

The detection of COMs in starless cores has been reported for decades. For example, [Matthews et al. \(1985\)](#) detected CH_3CHO in the starless cores TMC-1 and L134N. [Friberg et al. \(1988\)](#) later detected CH_3OH in the same regions. [Bacmann et al. \(2012\)](#) reported the presence of CH_3CHO , CH_3OCH_3 , and HCOOCH_3 in the starless core L1689B. The other starless (including prestellar) cores reported to host detectable COMs include H-MM1 ([Harju et al. 2020](#)), IRAS 16293E ([Spezzano et al. 2025](#); [Scibelli et al. 2025](#)), L429-C ([Taillard et al. 2023](#)), L1498 ([Tafalla et al. 2006](#)), L1544 ([Bizzocchi et al. 2014](#); [Vastel et al. 2014](#); [Jiménez-Serra et al. 2016](#); [Spezzano et al. 2016, 2017](#); [Lin et al. 2022](#)), L1517B ([Tafalla et al. 2006](#); [Megías et al. 2023](#)), L1521E ([Nagy et al. 2019](#); [Spezzano et al. 2020](#); [Scibelli et al. 2021](#)), TMC-1 CP ([Soma et al. 2015](#); [Soma et al. 2018](#)), TUKH122 ([Ohashi et al. 2018](#)). In recent years, COM surveys targeting a larger number of starless cores have begun to emerge. For example, [Scibelli & Shirley \(2020\)](#) investigated COM compositions in 31 starless cores within the L1495–B218 filament of the Taurus molecular cloud. [Scibelli et al. \(2024\)](#) conducted a survey toward 35 starless cores in the Perseus cloud. Interestingly, both of them found a 100% detection rate of CH_3OH , suggesting the prevalence of COMs in starless cores.

In addition to investigating the occurrence of COMs, another important line of research focuses on their spatial distributions. [Tafalla et al. \(2006\)](#) found that in L1498 and L1517B, CH_3OH exhibit a non-uniform, ring-like morphology that surrounds the dust continuum and N_2H^+ emission. A similar morphology of CH_3OH has also been reported in, for example, L1544 ([Bizzocchi et al. 2014](#); [Vastel et al. 2014](#); [Jiménez-Serra et al. 2016](#)), TUKH122 ([Ohashi et al. 2018](#)), H-MM1 ([Harju et al. 2020](#)), and five cores in the Orion cloud ([Hsu et al. 2025a](#)). This ring-like structure is thought to be the result of molecular depletion in the densest regions of the cores ([Tafalla et al. 2006](#); [Jiménez-Serra et al. 2016](#)). Subsequent studies showed that not only CH_3OH but also other COMs tend to be more abundant in the outer layers of the core, rather than at the continuum peak ([Jiménez-Serra et al. 2021](#); [Megías et al. 2023](#)). Finally, different distributions between CH_3OH and the carbon-chain molecules were also observed in L1544 ([Spezzano et al. 2016, 2017](#)) and toward a sample of six starless cores (L1521E, HMM-1, OphD, B68, L429, and L694-2, [Spezzano et al. 2020](#)). Differences in exposure to the interstellar radiation field (ISRF) have been suggested to cause such spatial segregation (e.g., [Jiménez-Serra et al. 2016](#); [Spezzano et al. 2017, 2020](#)).

The presence of gaseous COMs requires a desorption mechanism since COMs are believed to be formed in the icy

mantles of dust grains (e.g., [Herbst & van Dishoeck 2009](#)). In protostellar cores, the commonly adopted mechanism is thermal desorption due to central protostar and shocks (e.g., [Velusamy et al. 2002](#); [Arce et al. 2008](#); [Oya et al. 2016](#); [Okoda et al. 2022](#); [Hsu et al. 2023, 2024](#); [Bouvier et al. 2025](#); [Hsu et al. 2025b](#)). However, in starless cores, the mechanism driving the presence of COM gas is still puzzling, despite the ample COM-detections in starless cores recently. The plausible desorption mechanisms in this case include reactive desorption ([Garrod et al. 2007](#); [Vasyunin & Herbst 2013](#); [Vasyunin et al. 2017](#); [Chuang et al. 2018](#); [Jin & Garrod 2020](#); [Garrod et al. 2022](#); [Borshcheva et al. 2025](#)), cosmic-ray-induced sputtering ([Dartois et al. 2020](#); [Wakelam et al. 2021](#)), and grain-grain collision shocks ([Dickens et al. 2001](#); [Soma et al. 2015](#); [Harju et al. 2020](#); [Lin et al. 2022](#); [Kalvāns & Silsbee 2022](#); [Hsu et al. 2025a](#)). Recently, [Hsu et al. \(2025a\)](#) identified shock interfaces highlighted by the N_2H^+ and CH_3OH spatial and spectral correlation in several starless cores and proposed a “turbulence-induced mass-assembly shock” scenario, bridging the ubiquitous turbulence activity and the common detection of CH_3OH in starless cores.

With the prevalence of COMs in starless cores readily revealed in the nearby low mass star forming Taurus and Perseus clouds, it is pertinent to expand such a census to the Orion molecular cloud. While being at a farther distance of 400 pc (as compared to Taurus at 150 pc and Perseus cloud at 300 pc) ([Lombardi et al. 2010](#); [Lombardi et al. 2011](#); [Zucker et al. 2018](#)), the Orion molecular clouds are known to experience stronger supersonic turbulence and more intense UV radiation fields (e.g., [Ha et al. 2022](#); [Xia et al. 2022](#)). Imaging observations similar to those in [Hsu et al. \(2025a\)](#) will allow one to further investigate the critical role of COMs in elucidating the physical and chemical processes within the starless cores in a cloud environment that may be different from those in the Taurus and Perseus clouds.

In this study, we present emission maps of N_2H^+ , CH_3OH , $\text{c-C}_3\text{HD}$, and CCS toward 16 starless cores in the Orion A and B molecular clouds, obtained with the Atacama Compact Array (ACA). We also conducted observations with the Yebes 40-m telescope, allowing a comparison between single-dish and interferometric measurements. Section 2 describes the observational setups and data acquisition. In Section 3, we characterize the general morphologies revealed in the ACA images. Section 4 presents a comparison of CH_3OH column densities derived from the ACA and Yebes data. In Section 5 and 6, we discuss the implications of our findings and summarizes our main results, respectively. In addition, we present in Appendix A additional detailed observational information and in Appendix B the overview of individual sources.

2. METHODS

Table 1. Information of the targets.

Name	Short Name	α (J2000)	δ (J2000)	Cloud	v_{LSR} (km s ⁻¹)	JCMT Name	Prestellar
G203.21-11.20E1	G203.21E1	05:53:51.40	+03:23:09.3	Orion B	10.62	G203.21-11.20East1	
G205.46-14.56M3	G205.46M3	05:46:06.10	-00:09:32.3	Orion B	10.16	G205.46-14.56North1 [†]	✓
G206.21-16.17N	G206.21N	05:41:39.30	-01:35:56.2	Orion B	9.90	G206.21-16.17North	
G206.21-16.17S	G206.21S	05:41:36.10	-01:37:47.6	Orion B	9.50	G206.21-16.17South	✓
G209.29-19.65N1	G209.29N1	05:35:00.80	-05:39:57.7	Orion A	8.44	G209.29-19.65North1	✓
G209.29-19.65S2	G209.29S2	05:34:53.80	-05:46:21.6	Orion A	7.44	G209.29-19.65South2	
G209.55-19.68N2	G209.55N2	05:35:07.50	-05:56:46.4	Orion A	8.15	G209.55-19.68North2	
G209.77-19.40E3	G209.77E3	05:36:36.00	-06:02:40.2	Orion A	7.76	G209.77-19.40East3	
G209.94-19.52N	G209.94N	05:36:11.40	-06:10:44.8	Orion A	8.17	G209.94-19.52North	✓
G210.37-19.53N	G210.37N	05:36:55.20	-06:34:35.2	Orion A	6.41	G210.37-19.53North	
G210.82-19.47N2	G210.82N2	05:38:00.00	-06:57:17.5	Orion A	5.20	G210.82-19.47North2	
G211.16-19.33N4	G211.16N4	05:38:56.10	-07:11:27.9	Orion A	4.45	G211.16-19.33North4	
G211.16-19.33N5	G211.16N5	05:38:46.00	-07:10:41.9	Orion A	4.27	G211.16-19.33North5	
G212.10-19.15N1	G212.10N1	05:41:21.30	-07:52:26.9	Orion A	3.99	G212.10-19.15North1	✓

NOTE— The coordinates are based on the continuum peak in our 3 mm observations. The only exception is G211.16-19.33N5 (G211.16N5) due to its nearby source HOPS-135 (05h38m45.347s, -07d10m56.04s). As a result, the coordinate of it here is the targeted coordinate, which was based on the ACA images of [Dutta et al. \(2020\)](#). The “JCMT Name” is the name of the source used in [Yi et al. \(2018\)](#). In column “Prestellar,” the “✓” marks sources identified as prestellar cores by [Sahu et al. \(2021\)](#).

2.1. Sample Selection

In this study, we investigated 16 cold cores drawn from the ALMA Survey of Orion PGCCs (ALMASOP) project ([Dutta et al. 2020](#)). The Planck Galactic Cold Clump (PGCC) catalogue provides an all-sky inventory of cold (10–20 K), dense clumps characterized by molecular hydrogen column densities of $N(H_2) > 10^{20} \text{ cm}^{-2}$ at an angular resolution of $5'$ ([Planck et al. 2016](#)). Based on follow-up observations with the James Clerk Maxwell Telescope (JCMT) using its Submillimetre Common User Bolometer Array-2 (SCUBA-2) instrument, 119 dense cores were identified by their $850 \mu\text{m}$ (dust continuum) emission within 96 PGCCs located in the Orion A, Orion B, and λ Orionis clouds ([Yi et al. 2018](#)). From these 119 cores, the ALMASOP project selected 72 compact and high-density sources and ultimately cataloged 23 starless cores and 56 protostellar cores ([Dutta et al. 2020](#)).

Our sample consists of 16 starless cores chosen from this ALMASOP catalogue, selected for their compact distribution (within $\sim 2,000$ au) in the 7-m ACA array data. All these cores were classified as starless by [Yi et al. \(2018\)](#) based on the absence of detections in the WISE bands (3.4–22 μm). In addition, all the cores exhibit strong N_2D^+ emission, indicative of their cold environments ([Kim et al. 2020](#)). A summary of the basic properties of these 16 targets is provided in Table 1. In addition, an overview of the targets is in Appendix B.1. These cores are distributed in the Orion A

or B clouds with a distance of ~ 400 pc ([Lombardi et al. 2011](#); [Kounkel et al. 2018](#)). The core masses range from 0.15 to $3.52 M_\odot$, reported by [Yi et al. \(2018\)](#) based on their $850 \mu\text{m}$ dust continuum emission. Among the 16 cores, five of them show compact structures and extremely high peak densities ($2\text{--}8 \times 10^7 \text{ cm}^{-3}$) and are thus classified as prestellar cores ([Sahu et al. 2021](#)). The remaining eleven exhibit flattened structures and lack continuum detections in the 12-m data.

2.2. Observations

2.2.1. ACA Band 3 (3 mm) Observations

The majority of this study is based on data obtained with the Atacama Compact Array (ACA) during ALMA Cycle 8 under Project ID #2021.2.00094.S (PI: Sheng-Yuan Liu), using Band 3 (3 mm) observations. The observations were carried out between July 17, 2022, and April 17, 2023. The executions were divided into two Scheduling Blocks (SBs): the first targeting 12 fields in the Orion A cloud, and the second targeting four fields in the Orion B cloud. The unprojected baseline lengths ranged from 3 to 16 k λ . The maximum recoverable scale of the observations was $60''$, and the final images achieved an angular resolution of approximately $20''$.

The receivers captured data across 12 spectral windows (SPWs.) In this study, we focus on four transitions, N_2H^+ $J = 1 - 0$, CCS $J = 8 - 7$, $N = 7 - 6$, $\text{CH}_3\text{OH } 2_{0,2} - 1_{0,1}$

Table 2. The molecular transitions in this report.

Formula	f_{rest} (GHz)	E_u (K)	g_u	A_{ij} (s^{-1})	Quantum Numbers
ACA					
N_2H^+	93.1734	4.47	27	$3.6287E-5$	$J = 1 - 0^\dagger$
CCS	93.8701	19.89	17	$3.7440E-5$	$J_N = 8_7 - 7_6$
CH_3OH	96.7414	6.96	20	$3.4075E-6$	$A, 2_{(0,2)} - 1_{(0,1)}$
c- C_3HD	107.4237	10.88	21	$4.4652E-5$	$3_{(1,3)} - 2_{(0,2)}$
Yebes					
CH_3OH	48.3725	2.32	12	$3.5502E-7$	$A, 1_{(0,1)} - 0_{(0,0)}$

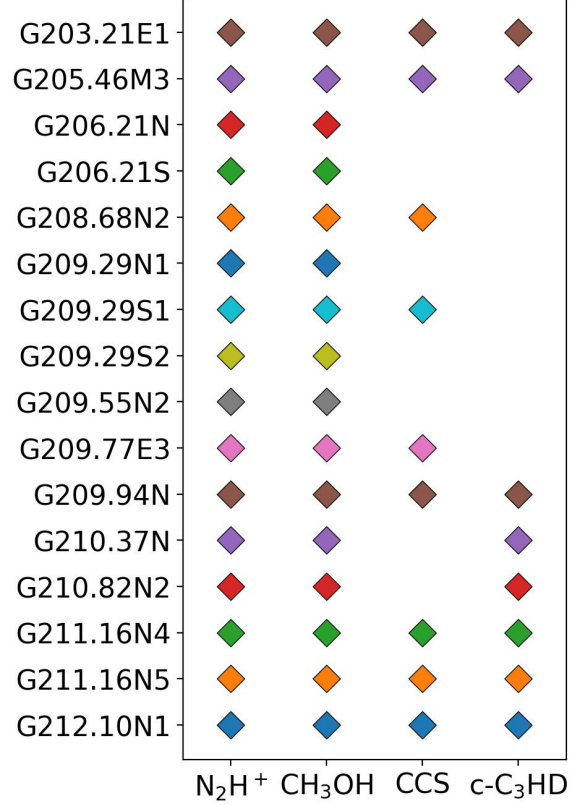
NOTE— E_u is the upper energy. f_{rest} is the rest frequency. E_u is the upper state energy. g_u is the upper state degeneracy. † The listed N_2H^+ transition contains the three hyperfine groups ($F_1 = 0-1, 2-1, 1-1$). We focus on the $F_1 = 0-1$ hyperfine group at 93.176 GHz and, under the assumption of optically thin emission, we multiplied it by a factor of nine when deriving the column densities.

References—The data were downloaded from the Splatalogue^a with their original references listed as follows. N_2H^+ : [Pagani et al. \(2009\)](#); CCS: [Yamamoto et al. \(1990\)](#); CH_3OH : [Xu & Lovas \(1997\)](#); c- C_3HD : [Bogey et al. \(1987\)](#).

^a <https://splatalogue.online/>

($E_u = 6.96$ K, hereafter CH_3OH -7K transition), and c- C_3HD $3_{1,3} - 2_{0,2}$ transitions. The detailed transition parameters are listed in Table 2. For N_2H^+ $J = 1 - 0$, we focus only on the hyperfine line group at 93.176 GHz ($F_1 = 0 - 1$) because (1) its hyperfine components are indistinguishable at our spectral resolution (61 kHz or 0.18 km s^{-1}), minimizing the effects of line blending in the channel maps, and (2) this group has the weakest intrinsic line strength of the three, making the emission comparatively less optically thick. The corresponding SPWs for the four molecules are #16, #18, #26, and #42. Please refer to Table A1 for the center frequencies, bandwidths, and the resolutions.

Imaging was performed using the `tclean` task in CASA 6.5.4 ([CASA Team et al. 2022](#)). The Briggs weighting with a robust parameter of 2.0 was applied for better illustrating the extended emission and improving the sensitivities. The imaging thresholds were 1.2 mJy for the full-band (~ 0.857 GHz) continuum and 100 mJy for individual channels (with a spectral resolution of 61 kHz per channel). The final images achieved a (geometric mean) beam size of $\sim 14''$ for the continuum and $\sim 18''$ for all datacubes, respectively. The resulting sensitivities were $0.5 \text{ mJy beam}^{-1}$ (0.2 mK) for the continuum and 25 mJy beam^{-1} (10 mK) for each channel. Tables A2 and A3 show

**Figure 1.** The ACA detection statistics of this study.

the beam parameters and noise levels for each source and SPWs.

2.2.2. Yebes Observation at Q Band

This study also utilized data obtained from the Yebes 40 m telescope under Project ID 22A010 (PI: Liu Xunchuan) in the Q band (31.00–50.50 GHz). This program targeted all 23 starless cores catalogued in the ALMASOP project, though the present study only uses those also observed with the ACA. The spectral resolution was 38 kHz. Each target was observed using the dual linear polarization Q-band receiver in frequency-switching mode with a standard throw of 10.52 MHz. The integration time per source was 180 minutes. Data reduction was performed using the CLASS program of the GILDAS¹ package ([Pety 2005](#)).

We focus on the CH_3OH $1_{(0,1)} - 0_{(0,0)}$ transition at 48.372456 GHz (with an upper-level energy of 2.69 K; hereafter, the CH_3OH -3K transition) at which frequency the spectral resolution of 38 kHz corresponds to a velocity resolution of $\sim 0.24 \text{ km s}^{-1}$. The angular resolution is approximately $36''$ at 48.4 GHz ([Tercero et al. 2021](#)). Table A3 shows the noise levels for each source.

¹ <https://www.iram.fr/IRAMFR/GILDAS/>

We conducted baseline subtraction for each source and extracted the spectrum centered at the expected line frequency with a 5 MHz window. The typical noise level in the extracted spectra is ~ 10 mK.

3. DETECTION AND MORPHOLOGY REVEALED BY INTERFEROMETRY

3.1. Detection

We applied the following processes for identifying the molecular detections. First, we adopted the datacube without primary beam correction so that the voxels across the entire image have similar noise levels. A molecule is considered detected if any voxel has a flux density above five times the noise level within a sub-cube centered on the target position within a circular region of $25''$ (10,000 au) and centered on the source v_{LSR} covering ± 3 km s $^{-1}$ in velocity.

Figure 1 shows the detection statistics for each species toward each source. As shown in Figure 1, we detected N_2H^+ and CH_3OH toward all the sources. On the other hand, we detected CCS and c- C_3HD toward only 10 and 8 among 16 sources, respectively. Seven of these sources have both CCS and c- C_3HD detections together (G203.21E1, G205.46M3, G209.94N, G210.82N2, G211.16N4, G211.16N5, and G212.10N1).

We found tentative evidence for environmental effects influencing the chemical composition on large scales. Several targets in our sample belong to the same PGCC, hence likely sharing similar environments. The cores within the same PGCCs have the same number in their short name, including G206.21N/S, G209.29S1/S2, and G211.16N4/N5. As shown in Figure 1, starless cores within the same PGCC tend to show generally consistent detections or non-detections of carbon-chain molecules. Figure 2 shows the Planck 857 GHz (350 μm) map of the Orion A and B clouds, with the target positions overlaid. White and magenta markers indicate sources with and without c- C_3HD detections, respectively. The targets with weak or no detections of c- C_3HD appear to be located near regions of bright 857 GHz emission ($F_\nu > 10^{-3.5}$ MJy sr $^{-1}$, see Figure 2). Since strong 857 GHz emission traces high dust column density and, consequently, high visual extinction, this suggests a possible correlation between dust extinction and the reduced abundance of carbon-chain molecules.

3.2. Morphology

To access the morphology, we generated integrated intensity (moment 0) maps for the four molecular species. For each molecule of each source, a consistent velocity integration interval was applied across the spatial plane. To determine this interval, we initially used the datacubes without primary beam correction. We then extracted sub-cubes covering ± 3 km s $^{-1}$ around the source v_{LSR} , within

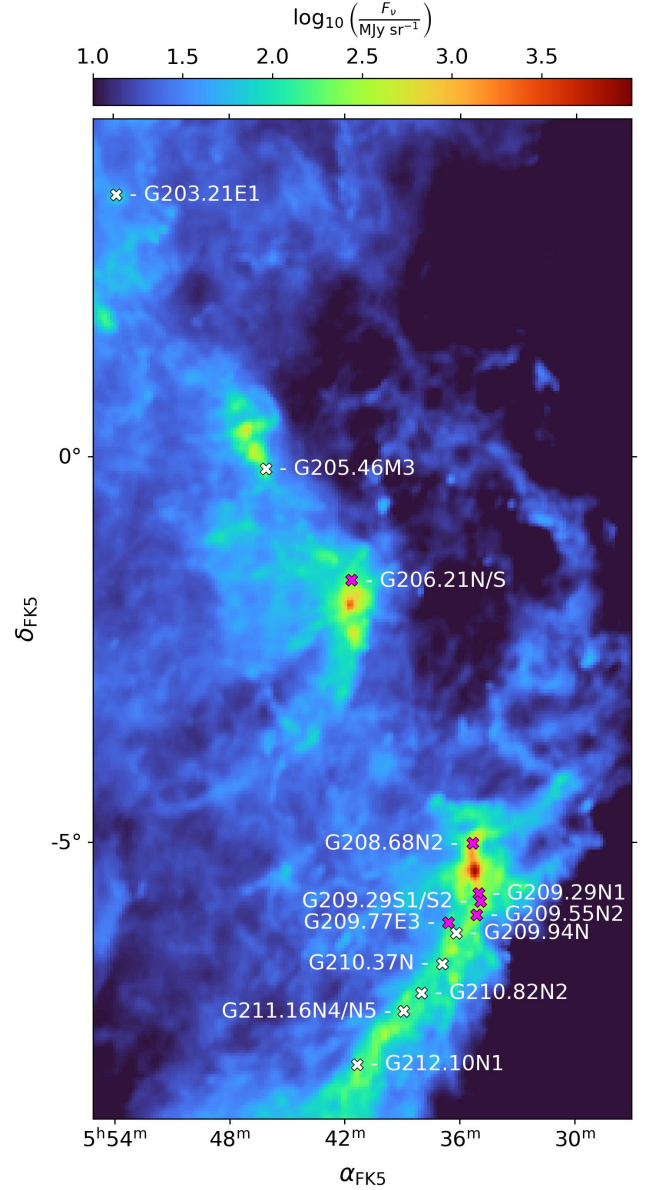


Figure 2. The Planck 857 GHz (350 μm) map of the Orion A and B clouds covering our targets. Each marker represents one clump in this study. The white and magenta markers illustrate the detection and non-detection of c- C_3HD , respectively. The white texts label the names of the clumps as well as the cores within.

a $25''$ (10,000 au) circular region centered on the target position. While the SNR for determining the molecular detection was five for a more robust criteria, integration interval was defined as the longest contiguous range of velocity channels in which the signal exceeded three times the noise level. The width of the integration interval is listed in Table B2. We finally applied the primary beam correction on the integrated maps. We include the resulting images derived from the aforementioned methods in Appendix B.2 for completeness (Figures B1 – B16). In the main text, we

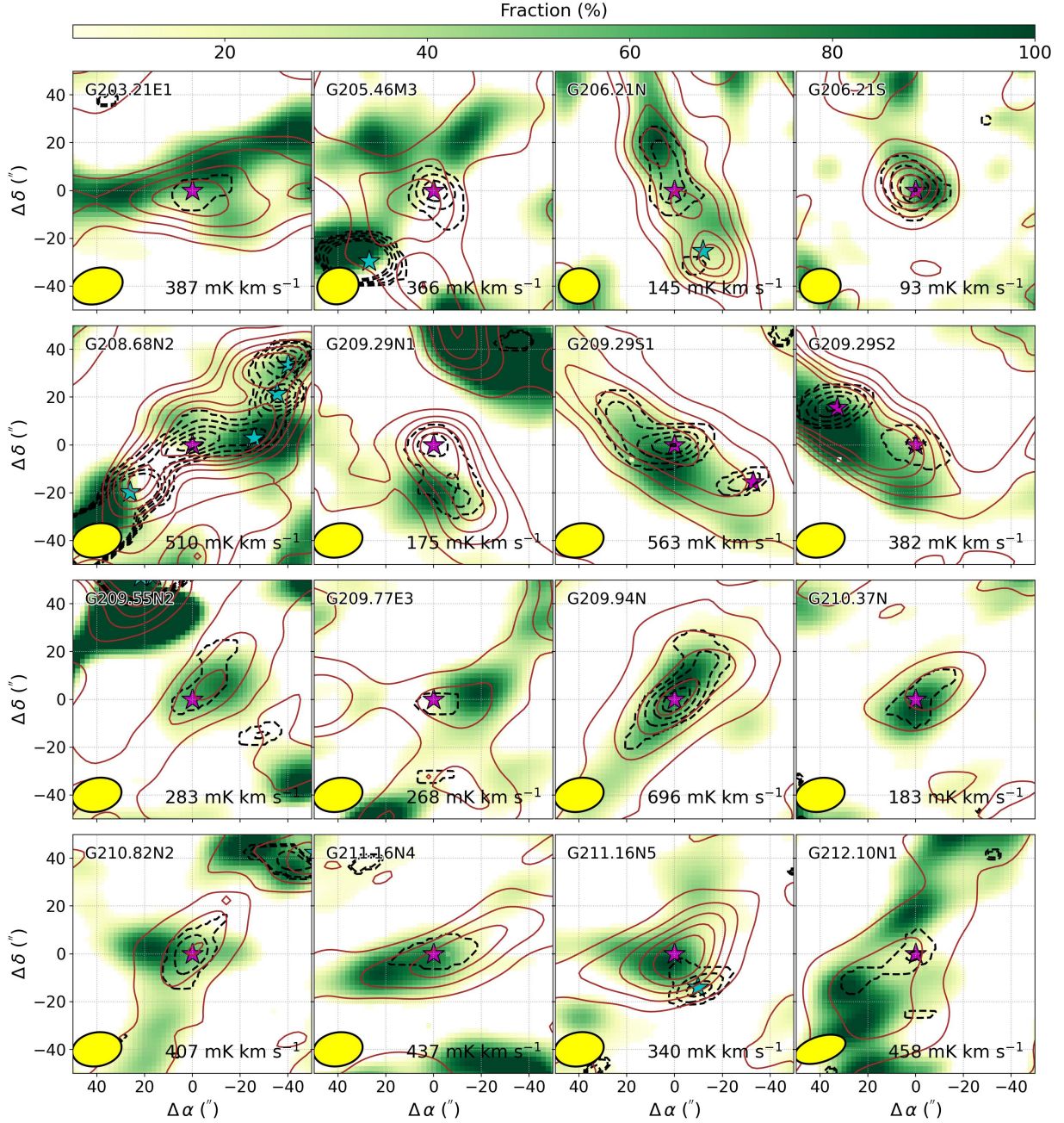


Figure 3. The integrated intensity images of CH_3OH (rasters) overlaid with that of N_2H^+ (brown solid contours) and 3 mm dust continuum (black dashed contours). The velocity range for deriving the integrated intensity images was fixed to $v_{\text{LSR}} \pm 1 \text{ km s}^{-1}$. The yellow ellipse at the lower left corner of each panel shows the synthesized beam of the rasters achieved by the ACA. The text at the lower right corner of each panel corresponds to the peak value for the global color bar. For five extremely dense starless cores, G205.46M3, G208.68N2, G209.94N, G209.29S1, and G212.10N1, the N_2H^+ contour levels are set at [5, 55, 105, 155, 205] σ ; for the remaining 11 cores, the contour levels are [5, 25, 45, 65, 85] σ with $\sigma \sim 7.5 \text{ mK km s}^{-1}$. The dust continuum contours are plotted at levels of [3, 6, 9, 12, 15] of the continuum noise levels, which are shown in Table A3. The magenta markers indicate the sources included in this study, with the target coordinate as the reference; the corresponding coordinates are listed in Table 1. The cyan markers indicate nearby sources reported by literature, which can be found in the overview description of each source in Appendix B.2.

present Figures 3 and 4, where a fixed integration interval of $v_{\text{LSR}} \pm 1 \text{ km s}^{-1}$ is adopted. The overall morphologies are consistent with those derived from the noise-based intervals.

As shown in Figure 3, N_2H^+ is known to trace cold and dense gas because CO, which would otherwise destroy N_2H^+ in the gas phase, becomes depleted in these environments (e.g., Bacmann et al. 2002). Most targets

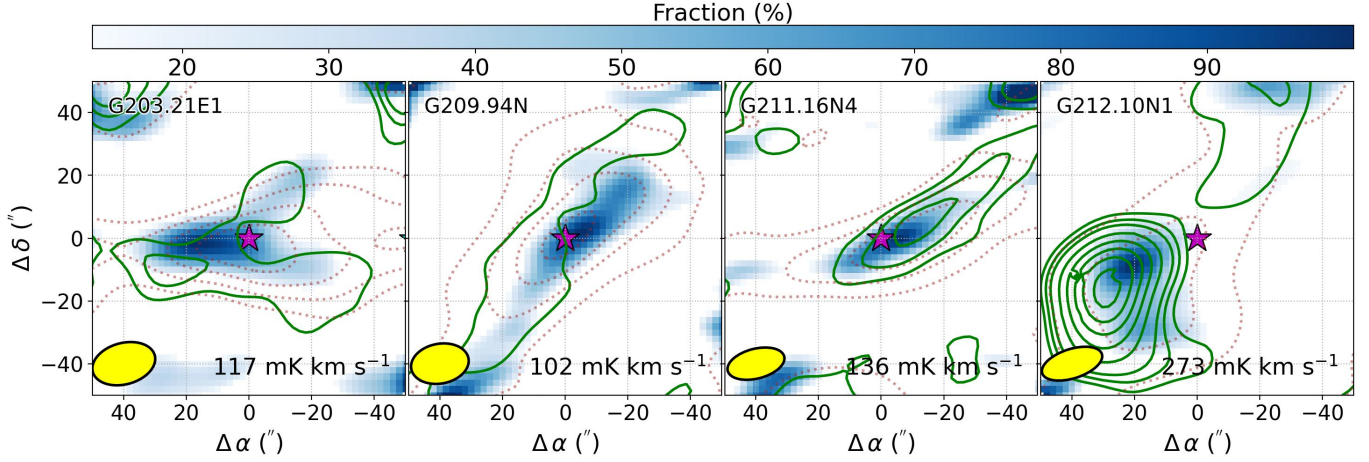


Figure 4. The integrated intensity images of c-C₃HD (rasters) overlaid with that of N₂H⁺ (brown dotted contours) and CCS (green solid contours). The velocity range for deriving the integrated intensity images was fixed to $v_{\text{LSR}} \pm 1 \text{ km s}^{-1}$. The yellow ellipse at the lower left corner of each panel shows the synthesized beam of the rasters achieved by the ACA. The text at the lower right corner of each panel corresponds the peak value for the global color bar. For G209.94N and G212.10N1, the N₂H⁺ contour levels are set at [5, 55, 105, 155, 205] σ ; for the remaining two cores, the contour levels are [5, 25, 45, 65, 85] σ . The CCS contours are plotted at levels of [5, 10, 15, 20, 25] σ . $\sigma \sim 7.5 \text{ mK km s}^{-1}$. The magenta markers indicate the sources included in this study, with the target coordinate as the reference; the corresponding coordinates are listed in Table 1. The cyan markers indicate nearby sources reported by literature, which can be found in the overview description of each source in Appendix B.2.

exhibit filamentary structures with a core near the center of the field, which we define as the primary starless core in this study. Some targets, such as G205.46M3, G206.21N, G208.68N2, and G209.29S2, show clearly identifiable multiple N₂H⁺ components within the field. Some of these companion cores are newly detected in our study, while others were previously identified as starless or protostellar cores by surveys such as Yi et al. (2018) and Dutta et al. (2020). Conversely, some known nearby YSOs are faint in radio emission and do not show corresponding N₂H⁺ components in our observations.

The spatial distribution of CH₃OH emission exhibits diverse and fragmented morphologies. It appears as core-like (e.g., G206.21S, G209.29N1, G209.55N2, G209.77E3, G210.37N); elongated and located on one side of the N₂H⁺ component (G203.21E1, G209.94N, G211.64N4); elongated but aligned with N₂H⁺ (G206.21N); extended (G209.29S1, G209.29S2, G210.82N2, G211.16N3); and complex (G205.46M3, G208.68N2, G212.10N1). In general, CH₃OH is distributed at the periphery of N₂H⁺, which was also observed in other cores (e.g., Tafalla et al. 2006; Bizzocchi et al. 2014; Vastel et al. 2014; Jiménez-Serra et al. 2016; Ohashi et al. 2018; Harju et al. 2020; Hsu et al. 2025a). Based on high-spatial- and spectral-resolution observations, Hsu et al. (2025a) proposed that CH₃OH traces turbulence-driven shocks of diffuse gas impinging onto dense filaments highlighted by N₂H⁺.

Both CCS and c-C₃HD are carbon-chain molecules, and in the six targets both CCS and c-C₃HD are consistently detected (Figure 1). The two carbon-chain molecules and

CH₃OH generally have different distributions, as shown in the figures of Appendix B.2. Even though they are often detected simultaneously, CCS and c-C₃HD generally show distinct spatial distributions. In Figure 4, we show the integrated intensity images of N₂H⁺, c-C₃HD, and CCS with a fixed velocity range of $v_{\text{LSR}} \pm 1 \text{ km s}^{-1}$ for the selected sources. These sources were selected due to their simultaneous detection of c-C₃HD, and CCS and without any nearby protostellar core. As shown in 4 (and corresponding panels in Figures B1, B11, B14, and B16), both CCS and c-C₃HD are located in the outer layers surrounding the dense gas component traced by N₂H⁺. The misaligned peaks between CCS and N₂H⁺ in four of our targets, G203.21E1, G298.68N2, G211.16N5, and G212.10N1, were also reported by Tatematsu et al. (2021). In addition to the segregation between CCS and N₂H⁺, as shown in Figure 4, CCS appears to trace a more extended outer layer than c-C₃HD, which is particularly evident in the first two sources (G203.21E1 and G209.94N).

Despite the limited number of detected transitions for each molecule, we estimated the column density associated with each core. Assuming optically thin and local thermodynamic equilibrium (LTE) with a fixed rotational temperature of 10 K (a typical gas temperature of starless cores, e.g., Scibelli et al. 2024), we derive the molecular column density maps for each species. For the CH₃OH-7K transition, Scibelli et al. (2024) reported optical thickness ($\tau > 1$) in one starless core. In our sample, the line peak brightness temperatures are all below or comparable to 1 K, which is significantly lower than the expected kinetic temperature of 10 K. On the basis that

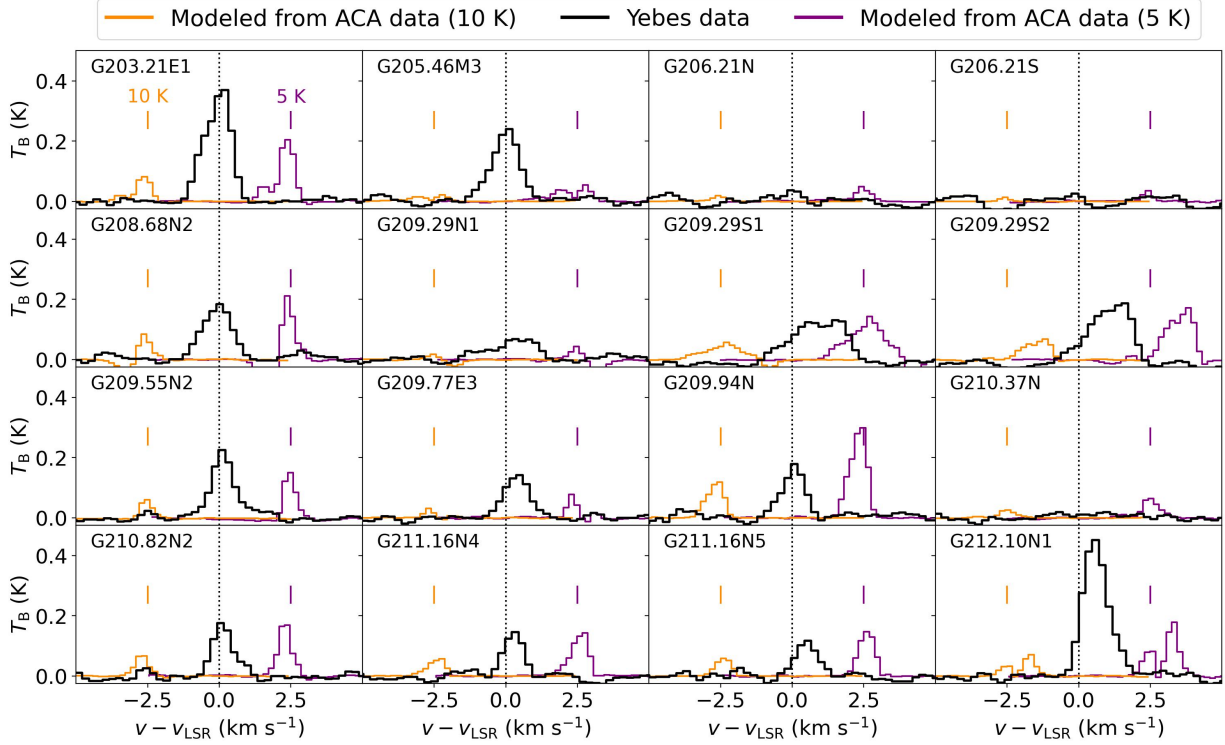


Figure 5. The spectra observed with Yebes 40-m observations (black) and modeled from ACA observations (orange and purple) for the CH₃OH-3K transition. The orange and purple spectra were estimated with given rotational temperature at 10 and 5 K, respectively, with a velocity offset of -2.5 and 2.5 km s⁻¹, respectively. We note that the angular separation between G209.29S1 and G209.29S2 is comparable to the Yebes beam size (36''), indicating that their emissions may be mutually contaminated.

CH₃OH emission is extended, the comparably low brightness temperature indicates that the emission in our sources is likely optically thin. The collisional rate coefficient of this transition at 10 K is $7.6 \times 10^{-11} \text{ cm}^3 \text{ s}^{-1}$ (Schöier et al. 2005), corresponding to a critical density of $4.5 \times 10^4 \text{ cm}^{-3}$. It is lower than or comparable to the typical gas densities in starless cores ($\sim 10^4\text{--}10^5 \text{ cm}^{-3}$), supporting the assumption of LTE. For N₂H⁺, the flux was multiplied by a factor of nine, as the $J = 1 - 0$ transition components ratio should be 1:5:3 for the three hyperfine transition groups (Daniel et al. 2006).

Appendix B.2 presents the equations and Figures B1 – B16 for the results. Moreover, we list in Table B2 the peak column densities for each species within a circular aperture of 25'' (10,000 au) centered on each target position. Note that the density of the column N_{tot}^p may be overestimated due to nearby bright sources within the 25'' aperture.

4. COMPARISONS WITH SINGLE-DISH OBSERVATIONS

As described in the previous section, CH₃OH generally appears to be spatially extended. The flux of such extended emission is likely underestimated due to interferometric spatial filtering. To assess the amount of missing flux, we compare our data with observations from the Yebes 40-m

telescope. The strongest CH₃OH transition covered by the observation was the CH₃OH-3K transition.

Figure 5 shows the CH₃OH spectra (black) obtained from the Yebes 40-m observations. Despite that we detected CH₃OH toward all the sources with the ACA observations, we did not see significant detection (signal-to-noise ratio, $\text{SNR} \geq 5$) in G206.21N, G206.21S, G209.29N1, and G210.37N in Yebes observations.

To assess the missing flux, we compared the CH₃OH lines observed with the Yebes 40-m single-dish telescope to the ACA interferometric observations. To do so, we modeled the CH₃OH-3K spectrum based on the directly observed CH₃OH-7K spectrum. First, we used the `imsmooth` task in CASA to convolve the ACA datacube to a circular beam comparable to the Yebes 40-m aperture (FWHM = 36'' at 48.4 GHz). We then extracted the CH₃OH-7K transition spectra at the pixel corresponding to the position targeted by the Yebes observations. Finally, we calculated the expected CH₃OH-3K spectra by rescaling the observed CH₃OH-7K spectra with the equations in Appendix B.2, assuming optically thin emission and LTE.

The modeled spectra are also shown in Figure 5. The orange and purple profiles represent the modeled spectra assuming rotation temperatures (T_{rot}) of 10 K and 5 K, respectively, with velocity offsets of -2.5 and +2.5 km

s^{-1} , respectively. A higher assumed rotational temperature results in a weaker modeled spectrum. In general, the modeled spectra are weaker than those observed with the Yebes 40-m telescope, regardless of whether T_{rot} is 10 K or 5 K. This difference suggests that the missing flux is significant in the ACA observations. In G206.21N, G206.21S, and G210.37N, the modeled spectra fall below the Yebes noise level, consistent with the non-detections in the Yebes observations.

To quantitatively evaluate the flux filtered out by the interferometer, we calculated the CH_3OH column densities at a common beam derived from the ACA and Yebes observations, with the equations in Appendix A under LTE, based on the observed CH_3OH -7K and CH_3OH -3K transitions, respectively. The results are shown in Figure 6. As illustrated in the figure, the ratio of the column density derived from the Yebes observations to that from the ACA data increases with increasing assumed rotational temperature.

At $T_{\text{rot}} = 10$ K, a typical gas temperature of starless cores (e.g., Scibelli et al. 2024), the observed column densities of the Yebes data can be up to ten times of those derived from the ACA observations. Scibelli & Shirley (2020) investigated CH_3OH in starless cores within the Taurus cloud and found that the typical CH_3OH gas kinetic temperature is about 7.5 K. At this temperature, six sources in our sample show column density ratios greater than $\sqrt{10}$, indicating that the ACA observations may be missing an order of magnitude of CH_3OH flux. These results highlight the significant amount of missing flux when observing CH_3OH emission with interferometry alone.

5. DISCUSSIONS

5.1. Chemical segregation related to CH_3OH

5.1.1. CH_3OH vs. N_2H^+

Our ACA observations show the general mismatched peak positions among N_2H^+ , CH_3OH , $\text{c-C}_3\text{HD}$, and CCS. On top of that, N_2H^+ is tracing the cold and dense core, while the other species seemingly reside in the outer layer of the core. The shell-like morphology of CH_3OH surrounding the cold gas tracers (e.g., N_2H^+) or dust in starless cores were also reported in the literature. For example, Tafalla et al. (2006) found that, in L1498 and L1517B, molecules such as CH_3OH and $\text{c-C}_3\text{H}_2$ fit with profiles having a sharp central hole. Bizzocchi et al. (2014) reported that in the prestellar core L1544, the CH_3OH emission resembles a non-uniform ring surrounding the dust peak. Vastel et al. (2014) applied the non-LTE analysis of the methanol lines in L1544 and shows that they are likely emitted at the border of the core at a radius of $\sim 8,000$ au. Jiménez-Serra et al. (2016) compare the molecular composition between the continuum peak and the CH_3OH peak in L1544 and found that the

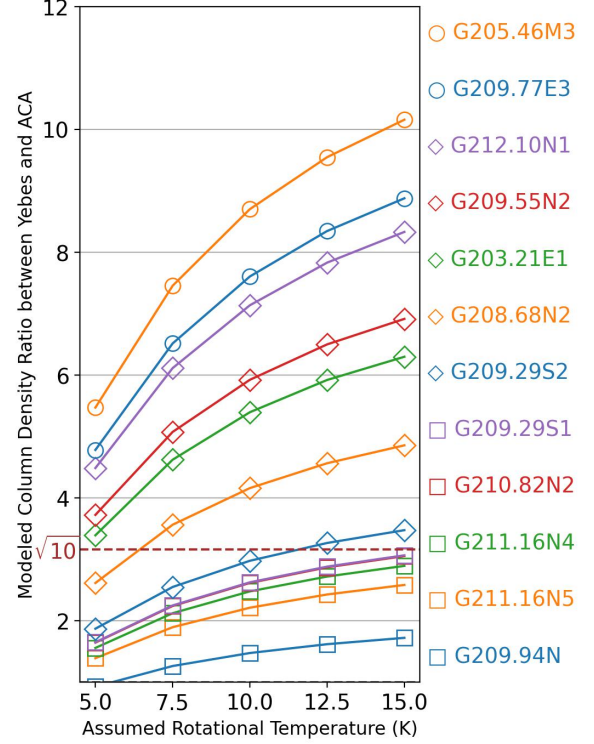


Figure 6. Variation of inferred CH_3OH column density ratios between Yebes and ACA observations as a function of assumed rotational temperatures. The Yebes and ACA values were estimated from the observed spectra of the CH_3OH -3K and CH_3OH -7K transitions, respectively. Each polyline represents one source. Only the 12 sources with CH_3OH detections in the Yebes observations are included in this plot. We note that the angular separation between G209.29S1 and G209.29S2 ($36''$) is smaller than the Yebes beam size ($36''$), indicating that their emissions may be mutually contaminated. The dashed line indicates a difference of one order of magnitude ($\sqrt{10}$).

COMs at the CH_3OH peak are overall more abundant than that at the continuum peak. Jiménez-Serra et al. (2016) proposed a scenario to explain the shell-like morphology of CH_3OH . In this scenario, three conditions must be met: (1) the density must be high enough for efficient CO freeze-out, allowing CH_3OH to form on grain surfaces; (2) the density must not be too high, so that gaseous CH_3OH is not significantly depleted; and (3) the visual extinction must be sufficiently large to shield CH_3OH from photodissociation by the external interstellar radiation field (ISRF). Together, these conditions suggest that gaseous CH_3OH can only survive within a shell-like layer at intermediate densities.

5.1.2. CH_3OH vs. carbon-chains molecules

Anti-correlations between CH_3OH and the two carbon-chain molecules (CCS and $\text{c-C}_3\text{HD}$) are observed in our studies (corresponding panels in Figures B1–B16). Chemical segregation between CH_3OH and $\text{c-C}_3\text{H}_2$ has been reported

in well-studied cores such as L1544 (Spezzano et al. 2016, 2017). Spezzano et al. (2016) suggested that such segregation between saturated (CH_3OH) and unsaturated (carbon chain) organics is driven by variations in the local ISRF. Regions exposed to stronger ISRF maintain a higher abundance of atomic carbon in the gas phase, favoring the formation of carbon-chain molecules such as $\text{c-C}_3\text{H}_2$. In contrast, in more shielded regions, carbon is predominantly locked in CO, allowing the efficient formation of COMs such as CH_3OH on dust grain surfaces. The illumination effect was also supported by Spezzano et al. (2020), who investigated the column density ratio between CH_3OH and $\text{c-C}_3\text{H}_2$, $N(\text{CH}_3\text{OH})/N(\text{c-C}_3\text{H}_2)$, in six starless cores embedded in environments with varying levels of shielding and at different evolutionary stages. For each target, the authors defined the “head” and “tail” based on the steep and shallow H_2 column density gradients, respectively. They found that the CH_3OH -to- $\text{c-C}_3\text{H}_2$ column density ratio is generally lower in the “head” than in the “tail,” suggesting that the chemical segregation is driven by uneven illumination.

5.2. The Ubiquitous CH_3OH Gas in Starless Cores

The presence of gaseous CH_3OH in star-forming regions is generally attributed to its formation on dust grain surfaces, followed by desorption into the gas phase (Herbst & van Dishoeck 2009), despite other pathways were also suggested (e.g., reaction of CH_3^+ with water ice, Nakai et al. 2023).

In the protostellar stage, gas-phase COMs are primarily produced through thermal desorption. As the temperature rises, COM molecules can be partially released from ice surfaces into the gas phase, and are fully desorbed when the temperature exceeds the ice sublimation threshold of ~ 100 K. A major heating source is the central protostar, which warms the inner envelope and creates a warm region rich in gaseous COMs, commonly referred to as a hot corino (e.g., Ceccarelli 2004; Hsu et al. 2023). Non-thermal desorption processes also play an important role. One such mechanism in protostellar sources is ice sputtering caused by energetic shocks. These shocks can originate from outflows (e.g., Arce et al. 2008; Hsu et al. 2024; Bouvier et al. 2025) or from envelope-to-disk accretion (e.g., Velusamy et al. 2002; Oya et al. 2016; Okoda et al. 2022; Hsu et al. 2025b). Shocks can also locally raise temperatures and trigger thermal desorption.

In the starless stage (including the prestellar stage), however, the absence of a central protostar, outflows, envelope, and disk structure makes the above-mentioned desorption scenarios unlikely and suggests the need for different mechanisms. These reactions, such as reactive desorption (e.g., Garrod et al. 2007; Vasyunin & Herbst 2013; Vasyunin et al. 2017; Chuang et al. 2018), cosmic-

ray-induced sputtering (Dartois et al. 2020; Wakelam et al. 2021), and shocks (e.g., Soma et al. 2015; Harju et al. 2020; Scibelli & Shirley 2020; Lin et al. 2022; Kalvāns & Silsbee 2022; Hsu et al. 2025a), can lead to the desorption of either COMs or their precursors. In reactive desorption, the desorption occurs naturally as a result of the exothermic reactions, such as those involved in the formation of methanol on grains. Cosmic-ray-induced sputtering occurs when cosmic rays impact solids, and the excitation of electrons leads to a brief thermal spike that can eject surface species. In addition to the two mechanisms mentioned above, the studies by Roberts et al. (2007) and Priestley et al. (2025) both addressed three other desorption mechanisms, H_2 formation on grains, direct cosmic-ray heating, and cosmic-ray-induced photodesorption.

Shocks may be caused by turbulent activity or mass accretion flows. In TMC-1 CP, Soma et al. (2015) proposed the clump-clump collision shock scenario as a possible mechanism for CH_3OH desorption. In H-MM1, Harju et al. (2020) suggested that CH_3OH is released as a result of grain-grain collisions induced by turbulence. Scibelli & Shirley (2020) found that the CH_3OH line profiles in their targeted starless cores could be explained by a combination of unresolved motions and supersonic turbulence. Lin et al. (2022) proposed that the enhancement of CH_3OH in L1544 is driven by slow shocks induced by accretion flows linked to the large-scale cloud dynamics. In this scenario, the extent of CH_3OH is primarily determined by the location of shocks, while environmental effects, such as the external illumination (Spezzano et al. 2016, 2020), are not necessarily in conflict with this interpretation. On another note, Spezzano et al. (2025) detected red- and blue-shifted components in addition to the primary velocity component of CH_3OH toward IRAS 16293E. They proposed that these shifted components do not originate from the core itself but instead arise from line-of-sight emission produced by shocks, likely associated with outflows from a nearby protostar system. This interpretation was subsequently supported by Scibelli et al. (2025).

Recently, under our ALMASOP project, Hsu et al. (2025a) identified shock interfaces between N_2H^+ and CH_3OH in several starless cores and proposed a “turbulence-induced mass-assembly shock” scenario. In this picture, magnetohydrodynamic (MHD) turbulence facilitates mass assembly in starless cores (Balsara et al. 2001; Ohashi et al. 2016; Keown et al. 2017), while the accompanying shocks drive CH_3OH desorption from icy grain mantles. The desorption may result either from localized temperature increases (i.e., thermal desorption) (e.g., Dickens et al. 2001; Soma et al. 2015) or from mechanical processes such as sputtering or grain disruption (i.e., non-thermal desorption) (e.g., Kalvāns & Silsbee 2022).

In our ACA observations, all the targeted starless cores exhibit detectable CH_3OH emission, even though four of them are not detected in the Yebes observations. This discrepancy likely arises from the larger beam size of the Yebes observations ($\sim 36''$) compared to the ACA observations ($\sim 16''$), despite their similar noise levels in brightness temperature (~ 10 mK). The ubiquity of CH_3OH in starless cores has also been reported in surveys toward the Taurus (Scibelli & Shirley 2020) and Perseus (Scibelli et al. 2024) molecular clouds. As all the three surveys (including this study) focus on low-/intermediate-mass cores, the ubiquity of CH_3OH suggests that desorption processes, whether thermal or non-thermal, are prevalent in these starless cores. Given the uniformly high detection rates under diverse physical conditions, detection statistics alone do not allow any desorption mechanism to be ruled out.

Although CH_3OH is commonly distributed near the surface of dense cores traced by N_2H^+ , our maps reveal that the former in general does not fully cover the latter (Figure 3). In other words, CH_3OH sometimes traces only one side of the filament (e.g., G203.21E1 and G209.29S1/S2) or appears as a localized spot near its surface. Such asymmetric distributions have often been attributed to uneven exposure to the ISRF, as discussed in Sect. 5.1.2. A potential indication of this effect in our study is the common asymmetric CH_3OH distribution in the five southern cores, G210.37N, G210.82N2, G211.16N4/N5, and G212.10N1. These five cores lie within four clumps that exhibit comparable large-scale dust distributions (the four white markers in Figure 2) and their CH_3OH emission generally appears on the eastern side of the N_2H^+ . This common asymmetry might result from stronger ISRF on the general western side of the clumps where the cores are embedded within, although we fail to identify promising stellar sources responsible for such enhanced (UV) radiation fields.

Under the turbulence-induced mass-assembly shock scenario, such asymmetric CH_3OH distributions reflect local turbulence activity. As described in Sect. 3, CH_3OH appears to trace diffuse gas components near the filament surface itself. This scenario naturally explains why CH_3OH exhibits substructures that are not seen in N_2H^+ . In this framework, the localized CH_3OH spots likely trace shock fronts at the interfaces between the diffuse and dense gas components, where mass flows converge.

5.3. The Extended CH_3OH Component inferred from the Missing Flux

Our comparison between the Yebes and ACA observations suggests that the ACA data can significantly underestimate the emitted CH_3OH flux. This underestimation points to the presence of a spatially extended component, potentially larger than $60''$ (the maximum recoverable scale of the

ACA). Images from single-dish observations are necessary to confirm this. We searched the literature for supporting evidence of such an extended component and found that, in L1544, the CH_3OH morphology indeed shows a superposition of an enhanced component on the eastern side of the dense core overlaid on a more extended emission structure. This is illustrated in Figure 1 of Spezzano et al. (2017) and Lin et al. (2022), both based on observations with the IRAM 30-m single-dish telescope. Since L1544 is a prestellar core, which is more evolved among starless cores, more sensitive single-dish surveys toward starless cores, including both prestellar and non-prestellar ones, are needed to further confirm this result.

A similar case was reported by Scibelli & Shirley (2020), who performed on-the-fly (OTF) mapping over $15' \times 15'$ regions containing starless cores in the Taurus molecular cloud. They detected methanol emission extending up to $\sim 15'$ ($\sim 1.2 \times 10^5$ au) in two regions, B10 and B211, which were classified as “less evolved” based on the absence of protostellar activity (Seo et al. 2015). Furthermore, Scibelli & Shirley (2020) found that starless cores within these less evolved regions tend to exhibit higher CH_3OH fractional abundances. They interpreted this trend as a consequence of depletion: in more evolved regions, cores are generally denser, leading to larger CH_3OH depletion zones.

It is intriguing that CH_3OH gas is detected in such diffuse regions. One possible explanation is that CH_3OH forms in situ on dust grain surfaces and subsequently desorbs. Alternatively, CH_3OH molecules could form and desorb in denser regions and then be transported into the surrounding diffuse gas. Both cases could be explained by the turbulence-induced shock scenario. In the former, CH_3OH may trace ongoing turbulent activity that could drive non-thermal desorption. In the latter, the emission might be related to the mixing between the cloud gas and the surrounding medium due to the instabilities near the surface with strong velocity shear (e.g., Kupilas et al. 2021). Future simulations that include both turbulent dynamics and the formation, desorption, and adsorption processes of CH_3OH may help to assess this possibility.

5.4. Segregation between Carbon-chain Molecules

Carbon-chain molecules can be efficiently produced in starless cores (e.g., Sakai & Yamamoto 2013, and the references therein). In the early diffuse-cloud stage, C^+ is the dominant form of carbon in the gas phase because interstellar UV radiation penetrates deeply. C^+ can then participate in a series of gas-phase reactions with species such as H_2 , e^- , H_3^+ , and C to form abundant carbon-chain molecules (see Figure 1 in Sakai & Yamamoto 2013). As the extinction increases, carbon becomes locked in the form of CO, and carbon-chain chemistry is suppressed.

In our observations, the two carbon-chain molecules, $c\text{-C}_3\text{HD}$ and CCS, are commonly detected together. Moreover, starless cores within the same clump generally show similar patterns of detection or non-detection for carbon-chain molecules. Clumps located in regions bright at 857 GHz generally appear deficient in carbon-chain chemistry, suggesting an anti-correlation between extinction and the presence of carbon-chain species. These trends are consistent with the current understanding of the chemical network of carbon-chain molecules, in which higher extinction leads to more carbon being locked in CO, thereby suppressing carbon-chain chemistry (e.g., Sakai & Yamamoto 2013; Taniguchi et al. 2024, and the references therein).

Interestingly, our observations show that although $c\text{-C}_3\text{HD}$ and CCS are frequently co-detected in the same sources, their emission exhibit different distributions. As described in Section 3 and shown in Figure 4, CCS appears to trace a more extended outer layer than $c\text{-C}_3\text{HD}$, which may reflect that $c\text{-C}_3\text{H}_2$ and CCS generally do not reside in the same structures. This contrasts with Spezzano et al. (2017), who found that in the prestellar core L1544, $c\text{-C}_3\text{H}_2$ (the main isotopologue) and CCS share the same emission peak. Admittedly, spatial filtering by interferometers may affect the observed morphology. The more centrally concentrated distribution of $c\text{-C}_3\text{HD}$ might also be explained by deuterium enhancement in dense, cold environments (e.g., Rodgers & Charnley 2001; Giers et al. 2022). Nevertheless, non-coincident distributions between $c\text{-C}_3\text{H}_2$ and CCS have been observed toward other starless cores through single-dish imaging. For example, based on the images presented by Spezzano et al. (2020) with the IRAM 30-m telescope, such non-coincident distributions are seen in Oph D, HMM1, and L694-2, and possibly in L429 as well, although this was not explicitly discussed in the text. Taken together, these results suggest that $c\text{-C}_3\text{H}_2$ (and $c\text{-C}_3\text{HD}$) and CCS generally exhibit distinct spatial extents.

To further examine whether the layered onion-shell like distribution of CCS and $c\text{-C}_3\text{HD}$ is due to excitation effects, we estimated their critical densities. As shown in Table 2, CCS and $c\text{-C}_3\text{HD}$ have comparable Einstein coefficients. The collision rate coefficient (γ_{ij}) of the CCS transition at 10 K is $\sim 2 \times 10^{-12} \text{ cm}^3 \text{ s}^{-1}$ in the LAMDA² (Schöier et al. 2005) database. Meanwhile, given the lack of $c\text{-C}_3\text{HD}$ collision rate in LAMDA, we adopted the value of $c\text{-C}_3\text{H}_2$ of the same transition ($\sim 9 \times 10^{-12} \text{ cm}^3 \text{ s}^{-1}$), which is significantly higher than that of CCS. Consequently, $c\text{-C}_3\text{HD}$ emission has a lower critical density than CCS emission and can trace more diffuse gas, which can not explain the observed morphology.

The layered distributions of CCS and $c\text{-C}_3\text{H}_2$ (and $c\text{-C}_3\text{HD}$) may arise from carbon-chain chemistry and the poorly understood sulfur chemistry. One possible explanation is the photo-dissociation of carbon-chain molecules, under the framework of photo-chemistry, Irradiation can prevent carbon from being efficiently retained in CO molecules, thereby enhancing carbon-chain chemistry. However, in regions most strongly exposed to irradiation, carbon-chain species themselves may be dissociated, ultimately suppressing the formation of larger chains. As a result, CCS becomes relatively abundant in the outer layers, while deeper layers can harbor more complex carbon-chain molecules such as $c\text{-C}_3\text{H}_2$ (and thus $c\text{-C}_3\text{HD}$). Within this framework, even larger carbon-chain molecules such as CCCS would be expected to show distributions more similar to $c\text{-C}_3\text{H}_2$.

Alternatively, CCS abundance in the outer layers may be enhanced through chemical processing of $c\text{-C}_3\text{H}_2$ (or $c\text{-C}_3\text{HD}$). Photo-chemistry could facilitate this pathway by producing enhanced S^+ in the outer layers, which in turn promotes the formation of CCS. According to the reactions in KIDA³ (KInetic Database for Astrochemistry, Wakelam et al. 2012, 2024) and Fig. 1 in Taniguchi et al. (2024), CCS can form from $c\text{-C}_3\text{H}_2$ via:



HCCCS^+ is also a parent species of CCCS:



As a result, within this framework, CCS and CCCS should share similar distributions. High-spatial resolution images or the line profiles of $c\text{-C}_3\text{H}_2$, CCS, and CCCS from single-dish observations will help verify the scenarios. Also, the density-based clustering method with a variety of features such as the intensity, velocity offset, and linewidth could possibly provide insights on the differentiation between molecular species, as demonstrated by Giers et al. (2025).

6. CONCLUSIONS

We conducted chemical surveys toward a sample of 16 starless cores in the Orion cloud selected from the ALMASOP catalog with ACA and Yebes observatories. We report the detection of N_2H^+ , CH_3OH , CCS, and $c\text{-C}_3\text{HD}$.

1. We report, in ACA observations, 100% detection rates for both N_2H^+ and CH_3OH , 62.5% for CCS, and 50% for $c\text{-C}_3\text{HD}$. This suggests that CH_3OH is prevalent in

² <https://home.strw.leidenuniv.nl/~moldata/>

³ <https://kida.astrochem-tools.org/>

starless cores, consistent with other surveys of starless cores in the Taurus and Perseus clouds. The ACA images reveal that CH_3OH and the two carbon-chain molecules generally trace the outer layers of the dense core traced by N_2H^+ , each exhibiting distinct spatial distributions.

2. Comparisons between the ACA and Yebes observations suggest that the ACA data may underestimate the CH_3OH flux by up to an order of magnitude, depending on the assumed methanol rotational temperature. These findings indicate the presence of an extended and flattened CH_3OH gas component.
3. We find that clumps located near dust-rich regions on larger scales tend to lack detections of carbon-chain molecules. This trend suggests that environmental effects at the clump scale, possibly linked to the strength of the interstellar radiation field, as discussed in the literature, can influence the organic chemical composition. In addition, we identify chemical segregation between the two carbon-chain species CCS and $\text{c-C}_3\text{HD}$ within individual starless cores. These distinct morphologies may likewise be understood in the context of photo-chemistry, highlighting the role of irradiation in regulating carbon-chain chemistry across both clump and core scales.

Software: Astropy (Astropy Collaboration et al. 2013, 2018, 2022), CASA (McMullin et al. 2007; CASA Team et al. 2022), CARTA (Comrie et al. 2021), GILDAS (Pety 2005).

ACKNOWLEDGMENTS

This paper makes use of the following ALMA data: ADS/JAO.ALMA#2021.2.00094.S. ALMA is a partnership of ESO (representing its member states), NSF (USA), and NINS (Japan), together with NRC (Canada), NSTC and ASIAA (Taiwan), and KASI (Republic of Korea), in cooperation with the Republic of Chile. The Joint ALMA Observatory is operated by ESO, AUI/NRAO, and NAOJ. Based on observations carried out with the Yebes 40 m telescope (22A010). The 40 m radio telescope at Yebes Observatory is operated by the Spanish Geographic Institute (IGN; Ministerio de Transportes y Movilidad Sostenible). X.-C. Liu and T. Liu acknowledges the supports by the National Key R&D Program of China (No. 2022YFA1603101). S.-Y. Hsu acknowledges supports from the Academia Sinica of Taiwan (grant No. AS-PD-1142-M02-2) and National Science and Technology Council of Taiwan (grant No. 112-2112-M-001-039-MY3). S.-Y. Liu acknowledges supports from National Science and Technology Council of Taiwan (grant No. 113-2112-M-001-004- and 114-2112-M-001-035-MY3).

Table A1. Information of the spectral windows.

SPW	f_c	BW	df	dv	Molecule
	(GHz)	(MHz)	(kHz)	(km s ⁻¹)	
#16	93.164	59	61	0.18	N ₂ H ⁺
#18	93.863	59	61	0.18	CCS
#26	96.732	59	61	0.18	CH ₃ OH
#42	107.003	117	122	0.37	c-C ₃ HD

NOTE— f_c is the center frequency. BW is the bandwidth. df and dv are the spectral resolution and the corresponding velocity resolution, respectively.

Table A2. Summary of the ACA observation beams.

Name	Short Name	3 mm	N ₂ H ⁺	CCS	CH ₃ OH	c-C ₃ HD
		(MAJ,MIN,PA)	(MAJ,MIN,PA)	(MAJ,MIN,PA)	(MAJ,MIN,PA)	(MAJ,MIN,PA)
G203.21-11.20E1	G203.21E1	15''.4, 12''.5, 76°	19''.5, 15''.8, -77°	16''.8, 13''.8, 76°	22''.0, 14''.8, -74°	20''.5, 13''.2, -75°
G205.46-14.56M3	G205.46M3	15''.4, 12''.1, 80°	18''.5, 15''.4, 73°	18''.1, 15''.4, 76°	17''.5, 15''.2, -73°	16''.4, 13''.1, -80°
G206.21-16.17N	G206.21N	15''.4, 12''.0, 80°	18''.7, 15''.7, -74°	17''.5, 15''.2, -83°	17''.0, 14''.8, -83°	16''.3, 13''.0, -81°
G206.21-16.17S	G206.21S	15''.4, 12''.0, 82°	18''.5, 15''.4, -75°	17''.7, 15''.1, -81°	17''.2, 14''.5, -83°	16''.2, 12''.7, -81°
G208.68-19.20N2	G208.68N2	19''.4, 9''.7, -73°	21''.3, 14''.5, -79°	21''.4, 14''.6, -77°	20''.7, 14''.1, -77°	18''.5, 12''.7, -78°
G209.29-19.65N1	G209.29N1	19''.3, 9''.6, -73°	21''.3, 14''.5, -80°	21''.3, 14''.6, -78°	20''.7, 14''.1, -78°	18''.6, 12''.7, -79°
G209.29-19.65S1	G209.29S1	19''.4, 9''.6, -73°	21''.3, 14''.5, -80°	21''.2, 14''.6, -78°	20''.8, 14''.1, -78°	18''.7, 12''.7, -79°
G209.29-19.65S2	G209.29S2	19''.4, 9''.6, -73°	21''.4, 14''.5, -80°	21''.2, 14''.6, -78°	20''.8, 14''.1, -78°	18''.8, 12''.7, -79°
G209.55-19.68N2	G209.55N2	19''.4, 9''.6, -73°	21''.4, 14''.5, -80°	21''.2, 14''.6, -78°	20''.8, 14''.1, -78°	18''.6, 12''.7, -79°
G209.77-19.40E3	G209.77E3	19''.3, 9''.6, -73°	21''.3, 14''.5, -80°	21''.2, 14''.6, -78°	20''.7, 14''.0, -78°	18''.5, 12''.7, -79°
G209.94-19.52N	G209.94N	19''.4, 9''.6, -73°	21''.4, 14''.5, -80°	21''.2, 14''.6, -79°	20''.8, 14''.0, -78°	18''.6, 12''.7, -80°
G210.37-19.53N	G210.37N	19''.3, 9''.6, -73°	21''.7, 11''.1, -76°	21''.2, 14''.5, -79°	20''.8, 14''.0, -79°	18''.5, 12''.7, -80°
G210.82-19.47N2	G210.82N2	19''.3, 9''.6, -74°	21''.6, 11''.0, -74°	21''.2, 14''.7, -80°	20''.8, 14''.1, -80°	18''.6, 12''.8, -81°
G211.16-19.33N4	G211.16N4	19''.3, 9''.6, -74°	21''.5, 14''.5, -82°	21''.0, 10''.4, -74°	20''.8, 14''.1, -80°	18''.6, 9''.5, -76°
G211.16-19.33N5	G211.16N5	19''.3, 9''.5, -74°	21''.3, 13''.7, -79°	21''.0, 10''.4, -74°	20''.8, 14''.2, -80°	19''.2, 9''.9, -78°
G212.10-19.15N1	G212.10N1	19''.2, 9''.5, -74°	23''.5, 14''.8, -79°	22''.3, 14''.8, -77°	22''.0, 10''.7, -72°	20''.0, 9''.3, -72°

NOTE—MAJ, MIN, and PA are the major axis size, minor axis size, and position angle.

APPENDIX

A. OBSERVATIONAL PARAMETERS

Tables A1, A2 and A3 show the ACA observational beam sizes and noise levels, respectively, for the continuum and each spectral window (SPW). In addition, the noise level of the Yebes observations is also listed in Table A3.

Table A3. Noise levels of the observations.

Name	Short Name	3 mm	N ₂ H ⁺	CCS	CH ₃ OH (ACA)	c-C ₃ HD	CH ₃ OH (Yebes)
		(mK)	(mK)	(mK)	(mK)	(mK)	(mK)
G203.21-11.20E1	G203.21E1	0.23	9.8	13.5	8.9	6.7	6.2
G205.46-14.56M3	G205.46M3	0.37	11.5	11.2	10.8	8.0	10.0
G206.21-16.17N	G206.21N	0.26	11.2	12.0	11.0	8.1	15.6
G206.21-16.17S	G206.21S	0.23	11.3	12.2	11.8	8.5	15.6
G208.68-19.20N2	G208.68N2	0.77	10.8	11.7	11.0	8.0	12.5
G209.29-19.65N1	G209.29N1	0.3	11.1	10.2	10.6	7.8	15.1
G209.29-19.65S1	G209.29S1	0.42	10.1	10.4	10.7	7.0	10.1
G209.29-19.65S2	G209.29S2	0.41	11.1	10.4	11.0	7.9	12.2
G209.55-19.68N2	G209.55N2	0.33	11.1	11.1	11.2	8.2	9.4
G209.77-19.40E3	G209.77E3	0.3	11.7	10.8	11.3	7.6	8.2
G209.94-19.52N	G209.94N	0.33	11.2	10.5	10.5	7.2	9.6
G210.37-19.53N	G210.37N	0.24	14.2	10.5	11.2	7.8	9.1
G210.82-19.47N2	G210.82N2	0.22	14.3	11.1	10.5	7.5	12.7
G211.16-19.33N4	G211.16N4	0.25	11.0	15.2	11.0	10.7	11.2
G211.16-19.33N5	G211.16N5	0.23	11.7	16.0	10.8	9.5	10.8
G212.10-19.15N1	G212.10N1	0.3	10.0	11.6	12.8	9.9	13.2

B. SOURCE OVERVIEW

B.1. Literature Review

All targets in this study were originally reported in [Yi et al. \(2018\)](#), which compared the overall properties of Planck Galactic Cold Clumps (PGCCs) in Orion A, Orion B, and the λ Orionis cloud based on 850 μ m dust continuum data from SCUBA-2 on the JCMT. As part of the sample, most of the cores were later observed by [Kim et al. \(2020\)](#) at 76–94 GHz using the Nobeyama 45 m telescope for molecules such as N₂D⁺, N₂H⁺, DNC, HN¹³C, CCS, HC₃N, and c-C₃H₂. Subsequently, these clumps were observed by ALMA as part of the ALMASOP project ([Dutta et al. 2020](#)), which further identified substructures within each clump. Following their inclusion in the ALMASOP catalog, (part of) this sample has been used in several studies, which are described as follows and summarized in Table B1. [Sahu et al. \(2021\)](#) presented a detailed analysis of the five densest starless cores, which show centrally concentrated regions with sizes of $\sim 2,000$ au and average densities of a few $\times 10^7$ cm⁻³. [Yi et al. \(2021\)](#) observed 80 cores (including nine starless cores in this study), distributed across Orion A, Orion B, and the λ Orionis clouds, and investigated the relationship between ultraviolet (UV) radiation fields and chemical composition in young stellar objects (YSOs). [Tatematsu et al. \(2021\)](#) observed 107 starless and prestellar cores, including six from this study, across Orion A, Orion B, and the λ Orionis clouds, investigating the emission lines of N₂H⁺, HC₃N, and CCS with the Nobeyama 45-m telescope. [Tatematsu et al. \(2022\)](#) studied inward motions in 30 starless (including all 16 cores in this study) and six protostellar cores using the data obtained from the Nobeyama 45 m radio telescope observations. The five sources in [Sahu et al. \(2023\)](#) and [Hsu et al. \(2025a\)](#) were adopted from [Sahu et al. \(2021\)](#), representing the densest starless cores in the ALMASOP sample. [Sahu et al. \(2023\)](#) modeled the density structures using observations from ALMA, ACA, and JCMT SCUBA-2. [Hsu et al. \(2025a\)](#) analyzed newly retrieved ALMA Band 3 data, discovered a shock interface between N₂H⁺ and CH₃OH, and proposed a turbulence-induced mass assembly framework, supporting the idea that turbulence drives mass accumulation and causes fragmented CH₃OH morphologies in starless cores. We note that the source G205.46–14.56M3 is referred to as G205.46–14.56North1 in [Yi et al. \(2018\)](#). Additional references focused on individual sources are discussed in the contextual descriptions of each object.

B.2. Integrated Intensity Images and Column Densities

Figures B1–B16 show the integrated intensity maps of N₂H⁺, CH₃OH, CCS, and c-C₃HD for each source. Table B2 lists the velocity integration interval we used. Rasters are colored green for detected molecules and purple for non-detections. Brown contours and black dashed contours represent the N₂H⁺ integrated intensity and the 3 mm dust continuum, respectively. For five particularly dense starless cores, G205.46M3, G208.68N2, G209.94N, G209.29S1, and G212.10N1, the N₂H⁺ contour levels

Table B1. Summary of sources included in literature. The “✓” labels the the sources included in the corresponding literature

Name	Short Name	Yi+18	Kim+20	Dutta+20	Sahu+21	Yi+21	Tatematsu+21	Tatematsu+22	Sahu+23	Hsu+25
G203.21-11.20E1	G203.21E1	✓	✓	✓		✓	✓	✓		
G205.46-14.56M3	G205.46M3	✓	✓	✓	✓			✓	✓	✓
G206.21-16.17N	G206.21N	✓	✓	✓		✓		✓		
G206.21-16.17S	G206.21S	✓		✓		✓		✓		
G208.68-19.20N2	G208.68N2	✓	✓	✓	✓	✓	✓	✓	✓	✓
G209.29-19.65N1	G209.29N1	✓	✓	✓				✓		
G209.29-19.65S1	G209.29S1	✓	✓	✓	✓			✓	✓	✓
G209.29-19.65S2	G209.29S2	✓	✓	✓			✓	✓		
G209.55-19.68N2	G209.55N2	✓	✓	✓		✓		✓		
G209.77-19.40E3	G209.77E3	✓	✓	✓		✓		✓		
G209.94-19.52N	G209.94N	✓	✓	✓	✓	✓	✓	✓	✓	✓
G210.37-19.53N	G210.37N	✓	✓	✓				✓		
G210.82-19.47N2	G210.82N2	✓	✓	✓				✓		
G211.16-19.33N4	G211.16N4	✓	✓	✓		✓		✓		
G211.16-19.33N5	G211.16N5	✓	✓	✓		✓	✓	✓		
G212.10-19.15N1	G212.10N1	✓	✓	✓	✓		✓	✓	✓	✓

References—Yi+18: [Yi et al. \(2018\)](#); Kim+20: [Kim et al. \(2020\)](#); Dutta+20: [Dutta et al. \(2020\)](#); Sahu+21: [Sahu et al. \(2021\)](#); Yi+21: [Yi et al. \(2021\)](#); Tatematsu+21: [Tatematsu et al. \(2021\)](#); Tatematsu+22: [Tatematsu et al. \(2022\)](#); Sahu+23: [Sahu et al. \(2023\)](#); Hsu+25: [Hsu et al. \(2025a\)](#);

are set at $[5, 55, 105, 155, 205]\sigma$. For the remaining 11 cores, the contour levels are $[5, 25, 45, 65, 85]\sigma$. The dust continuum contours are plotted at levels of $[3, 6, 9, 12, 15]\sigma$. The cyan markers indicate known nearby sources reported by literature. The magenta markers indicate the sources included in this study and the coordinates are listed in Table 1. Each panel includes two color bar labels: the upper label indicates the integrated intensity, while the lower label shows the corresponding column density.

The column densities were calculated as follows. First, assuming optically thin and local thermodynamic equilibrium (LTE), we derive the upper upper state column density N_u from the integrated intensity of transition in terms of the products of brightness temperature and velocity W via:

$$N_u = \frac{8\pi k_B \nu^2}{hc^3 A_{ul}} W, \quad (\text{B1})$$

where ν is the frequency and A_{ul} is the Einstein A coefficient of the transition. We then derived the total column density N_{tot} via:

$$\ln \left(\frac{N_u}{g_u} \right) = \ln \left(\frac{N_{\text{tot}}}{Z} \right) - \frac{E_u}{k_B T_{\text{rot}}}, \quad (\text{B2})$$

where g_u is the upper state degeneracy, T_{rot} is the rotational temperature, and Z is the partition function at T_{rot} . Table B2 lists the peak of the derived column density (N_{tot}^p) within a $25''$ (10,000 au) circular aperture centered on the target position.

Table B2. The velocity integration interval (Δv) used to derive the integrated intensity maps and the peak of the resulting column density (N_{tot}^p) within $25''$ (10,000 au). The integration interval (Δv) is defined as the longest continuous range of velocity channels where the signal exceeds three times the rms noise level. The peak column density (N_{tot}^p) is measured within a $25''$ (10,000 au) circular aperture centered on the target position. Note that the listed N_{tot}^p may be overestimated due to nearby bright sources within the $25''$ aperture.

Name	Short Name	N ₂ H ⁺		CCS		CH ₃ OH		c-C ₃ HD	
		Δv	N_{tot}^p	Δv	N_{tot}^p	Δv	N_{tot}^p		
		(km s ⁻¹)	(cm ⁻²)	(km s ⁻¹)	(cm ⁻²)	(km s ⁻¹)	(cm ⁻²)	(km s ⁻¹)	(cm ⁻²)
G203.21-11.20E1	G203.21E1	1.97	5.6×10^{12}	1.95	1.3×10^{12}	2.27	1.9×10^{13}	2.05	1.2×10^{12}
G205.46-14.56M3	G205.46M3	2.56	1.1×10^{13}	1.17	8.9×10^{11}	3.41	1.8×10^{13}	1.36	3.3×10^{11}
G206.21-16.17N	G206.21N	1.77	6.4×10^{12}	2.64	6.9×10^{12}
G206.21-16.17S	G206.21S	1.18	7.8×10^{12}	0.94	3.8×10^{12}
G208.68-19.20N2	G208.68N2	2.75	2.8×10^{13}	0.97	8.4×10^{11}	2.65	2.4×10^{13}
G209.29-19.65N1	G209.29N1	2.94	8.4×10^{12}	2.46	8.6×10^{12}
G209.29-19.65S1	G209.29S1	3.93	1.3×10^{13}	0.98	5.1×10^{11}	4.54	1.6×10^{13}
G209.29-19.65S2	G209.29S2	3.92	9.8×10^{12}	3.59	2.4×10^{13}
G209.55-19.68N2	G209.55N2	1.57	3.9×10^{12}	1.32	1.1×10^{13}
G209.77-19.40E3	G209.77E3	1.77	2.8×10^{12}	0.78	5.1×10^{11}	1.71	1.3×10^{13}
G209.94-19.52N	G209.94N	1.96	1.3×10^{13}	1.56	7.1×10^{11}	2.08	3.3×10^{13}	2.38	9.6×10^{11}
G210.37-19.53N	G210.37N	1.37	4.0×10^{12}	1.89	8.3×10^{12}	1.70	4.9×10^{11}
G210.82-19.47N2	G210.82N2	1.38	4.6×10^{12}	1.70	1.9×10^{13}	1.36	6.2×10^{11}
G211.16-19.33N4	G211.16N4	1.57	4.7×10^{12}	1.56	2.2×10^{12}	2.65	2.0×10^{13}	1.71	1.3×10^{12}
G211.16-19.33N5	G211.16N5	2.16	9.3×10^{12}	1.17	1.2×10^{12}	1.89	1.6×10^{13}	2.05	5.6×10^{11}
G212.10-19.15N1	G212.10N1	1.97	6.1×10^{12}	2.33	6.3×10^{12}	2.64	2.2×10^{13}	2.04	2.8×10^{12}

B.2.1. G203.21-11.20E1 (G203.21E1)

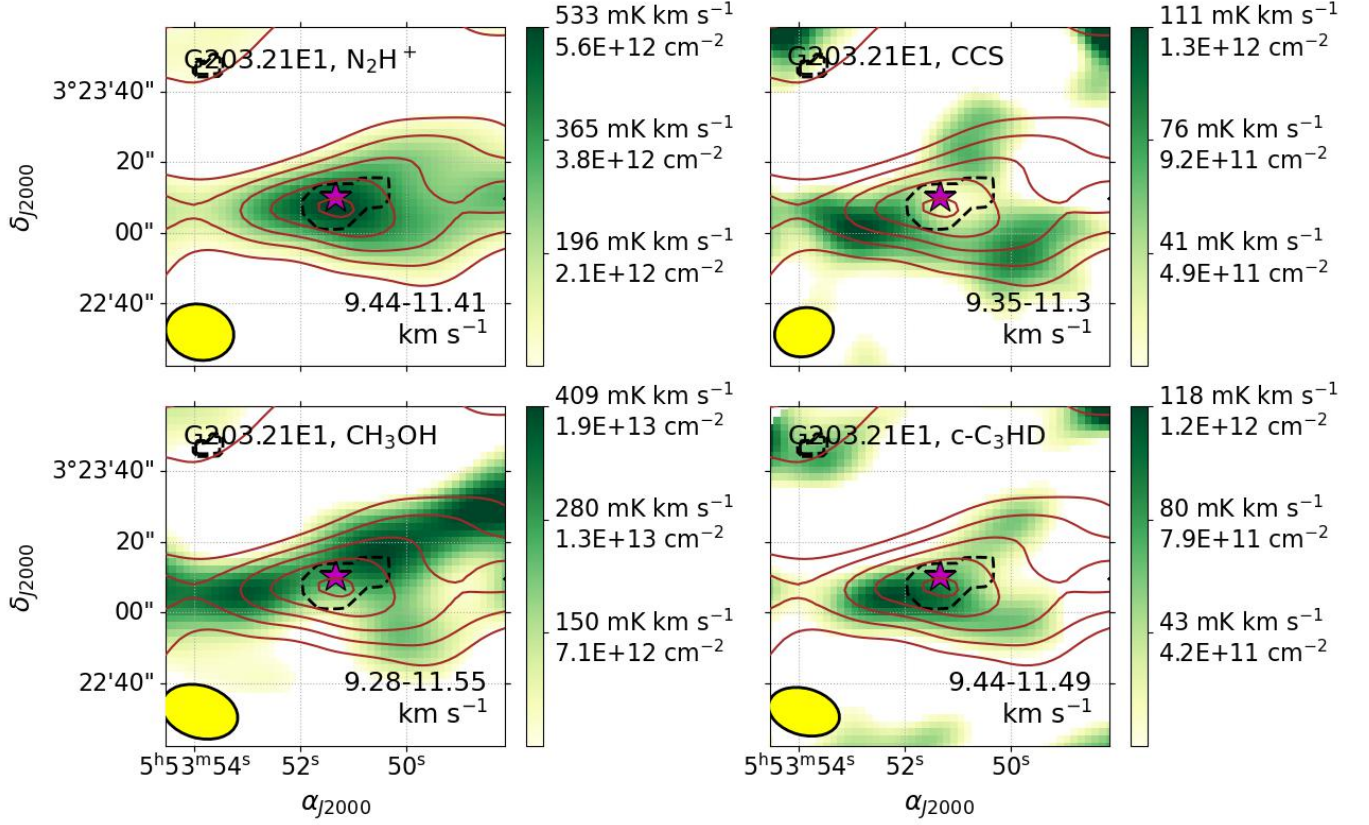


Figure B1. Integrated intensity images of G203.21-11.20E1 (G203.21E1). Please see the context in Appendix B.2 for the captions.

This source was not detected in ALMA 12-m data of ALMASOP project Dutta et al. (2020). Another starless core, G203.21-11.20E2, is located at the east of this source with a separation of $\sim 2''$. The distribution of N₂H⁺ resembles an isosceles acute triangle, with its acute angle pointing east and the two equal sides extending toward the north and south. A particularly strong molecular anti-correlation is observed in this source: CH₃OH is concentrated on the northern side, c-C₃HD resides on the southern side, and CCS appears as two distinct features located farther south, beyond the c-C₃HD emission region.

B.2.2. G205.46-14.56M3 (G205.46M3)

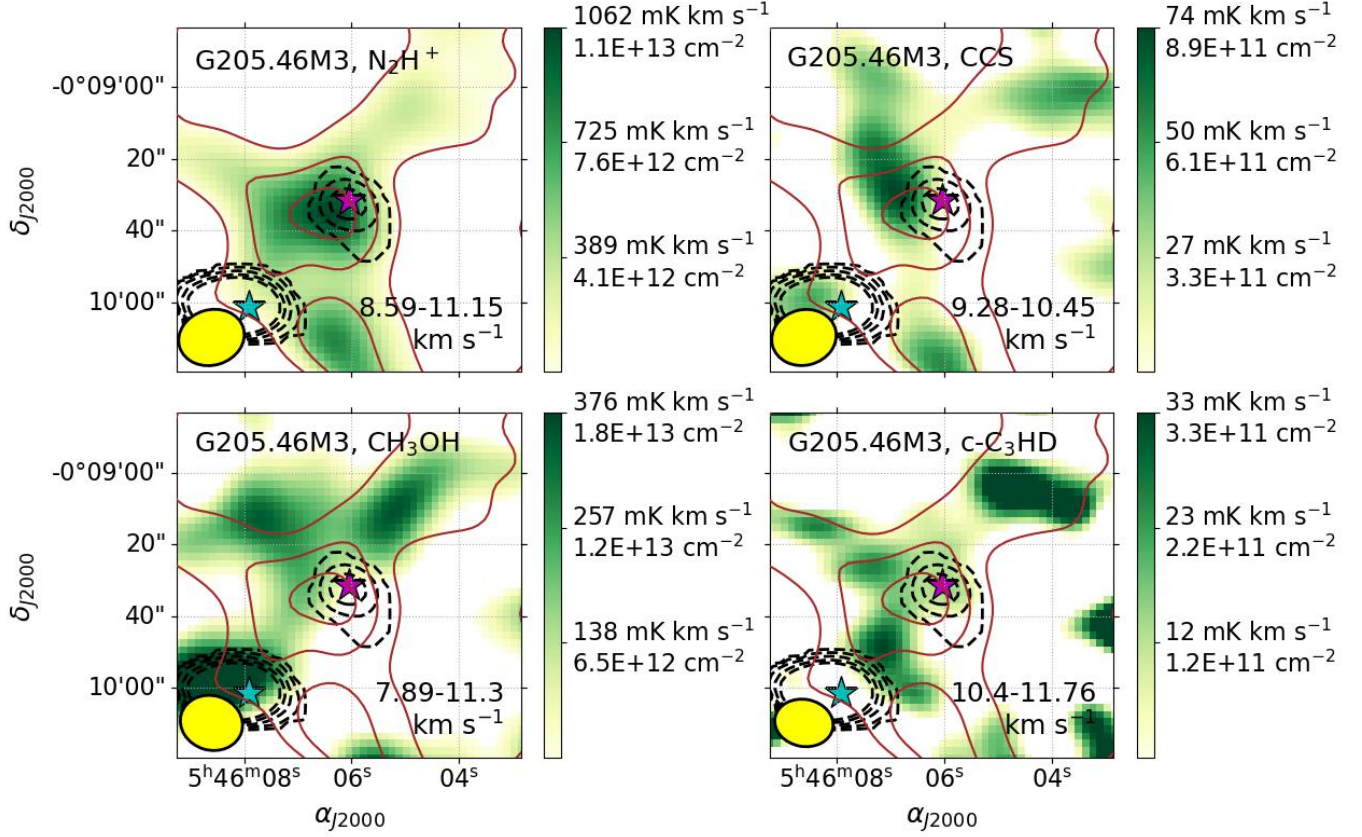


Figure B2. Integrated intensity images of G205.46-14.56M3 (G205.46M3). The texts on each panel green rasters label the source short name and the molecular species of the images. Please see the context in Appendix B.2 for the captions.

The clump G205.46–14.56M3 was referred to as G205.46–14.56North1 in the JCMT survey reported by Yi et al. (2018). Another protostellar core, G205.46–14.56M2 (also known as G205.46–14.56North2), which harbors HOPS-387 and HOPS-386, is located to the southeast, with a projected separation of approximately $30''$. Sahu et al. (2021) reported that G205.46–14.56M3 is fragmented into two substructures (B1 and B2) on a scale of $\sim 1,000$ au. Lin et al. (2025) detect $o\text{-H}_2D^+$ toward substructure B1 with an elevated N_2D^+/N_2H^+ , tracing advanced deuteration. As demonstrated by Lin et al. (2025), A time-dependent, deuteration-focused chemo-dynamical model reproduces these observables if the core assembles on a free-fall timescale, suggestive of turbulent core fragmentation.

The morphology of the molecular tracers in G205.46–14.56M3 is complex. The N_2H^+ emission peaks slightly east of the continuum peak and extends toward the northwest, northeast, and south. The CH_3OH , c- C_3H_2 , and CCS emissions associated with the clump appear as two extended components located on the northeast and northwest sides of the core. The two CH_3OH components exhibit comparable column densities; c- C_3H_2 is stronger in the northwest, while CCS is more prominent in the northeast.

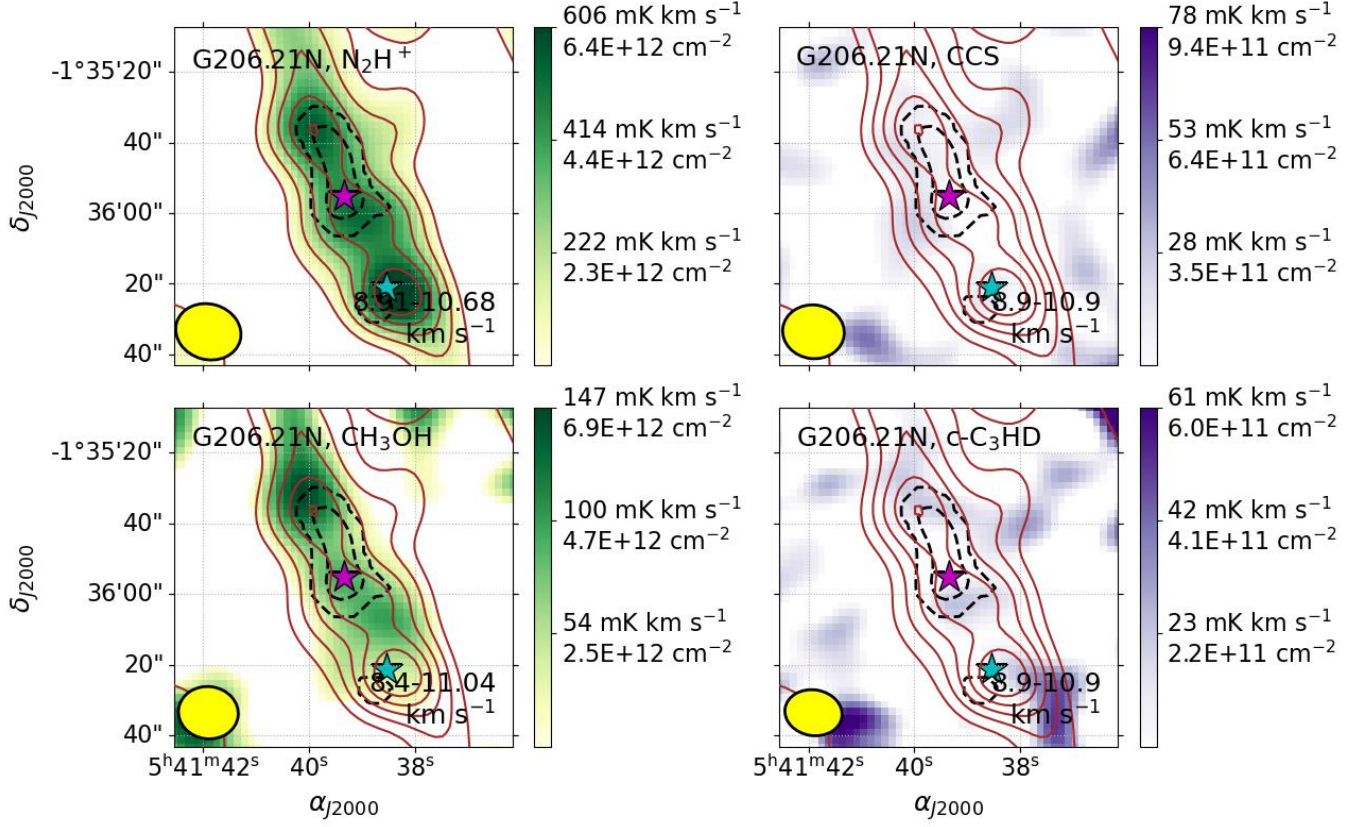
B.2.3. *G206.21-16.17N (G206.21N)*

Figure B3. Integrated intensity images of G206.21-16.17N (G206.21N). Please see the context in Appendix B.2 for the captions.

Overall, this clump exhibits a north–south elongation, and the N_2H^+ emission is resolved into three features: northern, middle, and southern. The southern feature corresponds to J054138.5–013621, a submillimeter source identified by Kirk et al. (2016), but it is not classified as a young stellar object. The CH_3OH emission generally follows the distribution of N_2H^+ , with the northern feature showing the strongest CH_3OH intensity. CCS and c- C_3HD are not detected in this clump.

B.2.4. G206.21-16.17S (G206.21S)

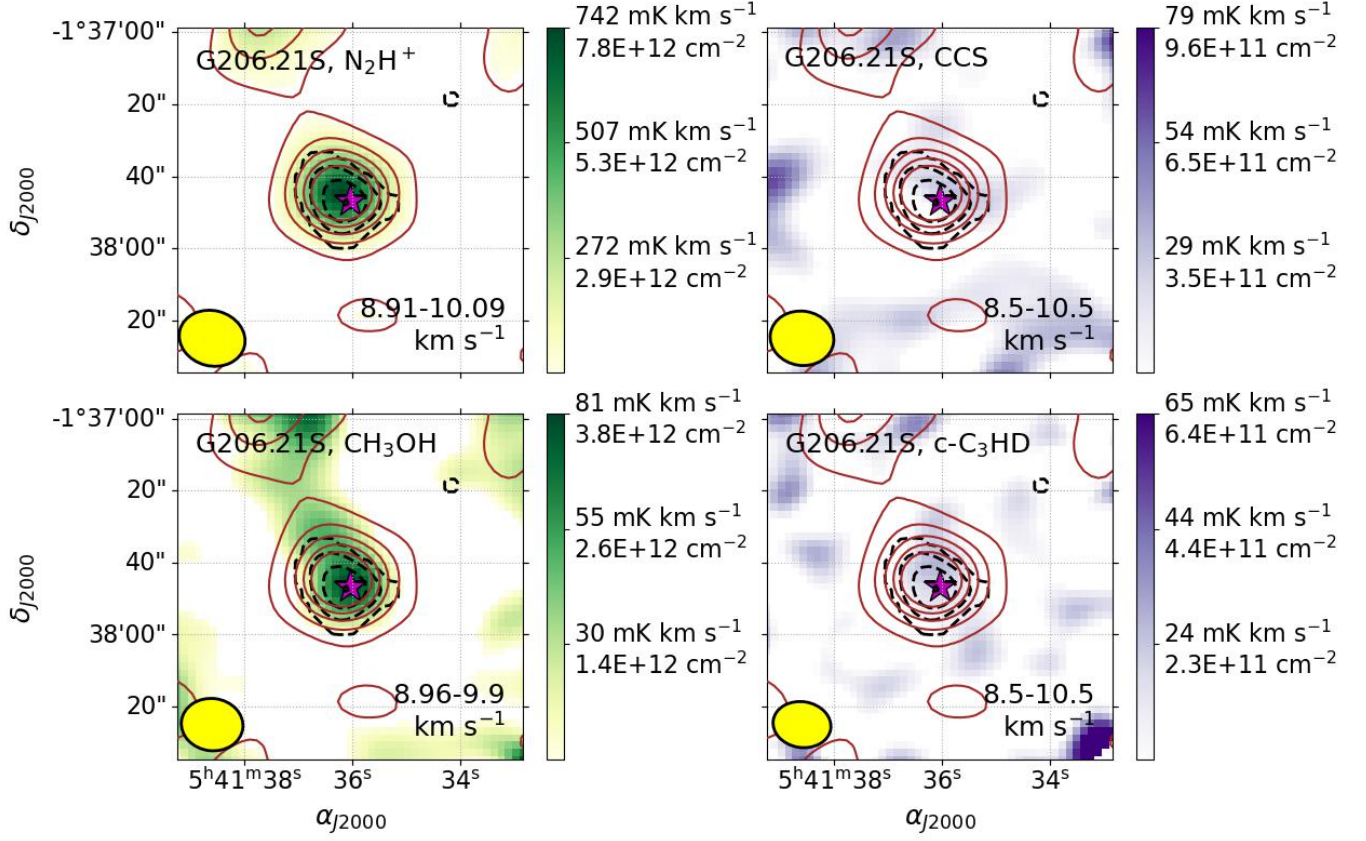


Figure B4. Integrated intensity images of G206.21-16.17S (G206.21S). Please see the context in Appendix B.2 for the captions.

In this clump, the N₂H⁺ emission exhibits a core-like morphology. The CH₃OH emission peaks near the N₂H⁺ peak and displays a tail extending toward the north. Neither CCS nor c-C₃HD is detected in this clump.

B.2.5. G208.68-19.20N2 (G208.68N2)

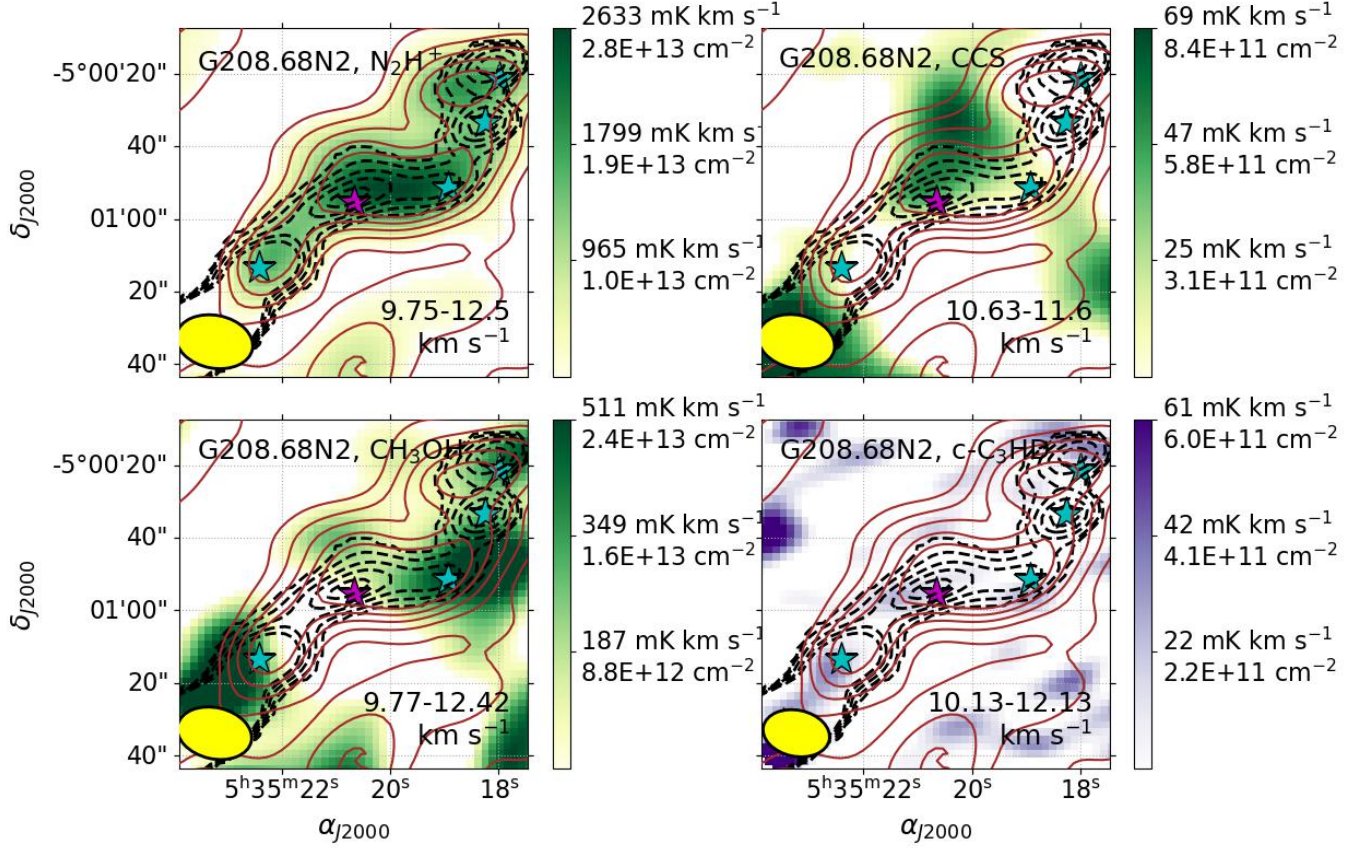


Figure B5. Integrated intensity images of G208.68-19.20N2 (G208.68N2). Please see the context in Appendix B.2 for the captions.

This clump, also known as OMC-3 MMS4, is located in the northern part of the OMC-3 region. Several sources are present within this field, arranged from northwest to southeast: HOPS 92 (OMC3 MMS 2, G208.68-19.20N1), HOPS 91 (OMC3 MMS 3), HOPS 89, HOPS 88 (OMC3 MMS 5), and HOPS 87 (OMC3 MMS 6, G208.68-19.20N1) (Furlan et al. 2016; Dutta et al. 2020). Hirano et al. (2024) reported an extremely dense and compact object embedded within this clump.

The N_2H^+ emission shows a strong peak associated with the starless core. However, due to the complex and crowded environment, it is difficult to confidently associate the other molecular components with specific structures. CH_3OH and CCS emissions appear to be located to the northeast of the clump, though their peak positions differ. The strong CH_3OH emission at the southeast side is likely associated with the hot corino in HOP 87 (OMC3 MMS 6, G208.68-19.20N1) field Hsu et al. (2024). No c- C_3HD emission is detected.

B.2.6. G209.29-19.65N1 (G209.29N1)

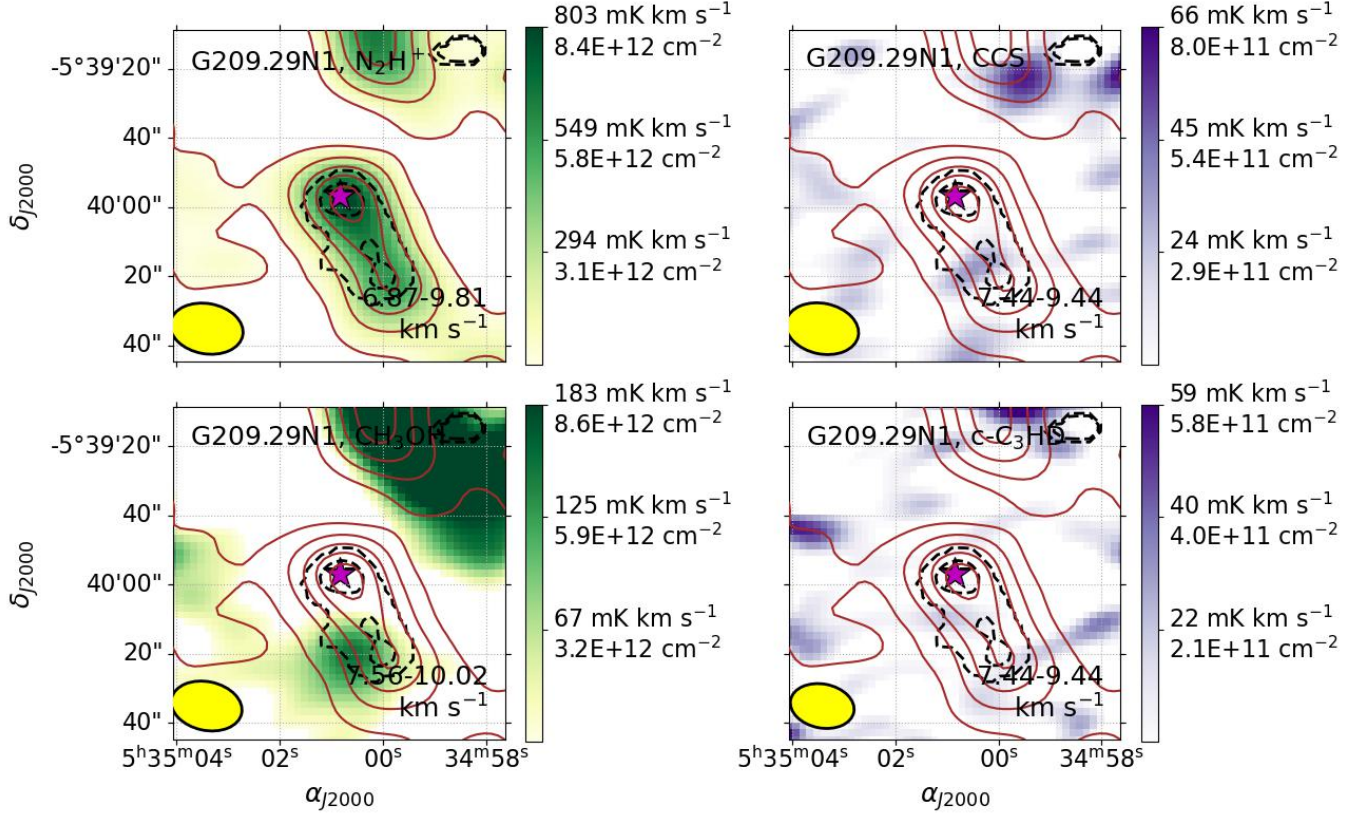


Figure B6. Integrated intensity images of G209.29-19.65N1 (G209.29N1). Please see the context in Appendix B.2 for the captions.

This clump is elongated in the northeast–southwest direction. The continuum emission appears to be fragmented into two features, located to the north and south. While the N_2H^+ emission does not show significant fragmentation, it exhibits a strong peak at the northern feature with a tentative tail extending southward. CH_3OH is distributed on the eastern side of the southern feature. Neither c- C_3H_2 nor CCS is detected.

B.2.7. G209.29-19.65S1 (G209.29S1)

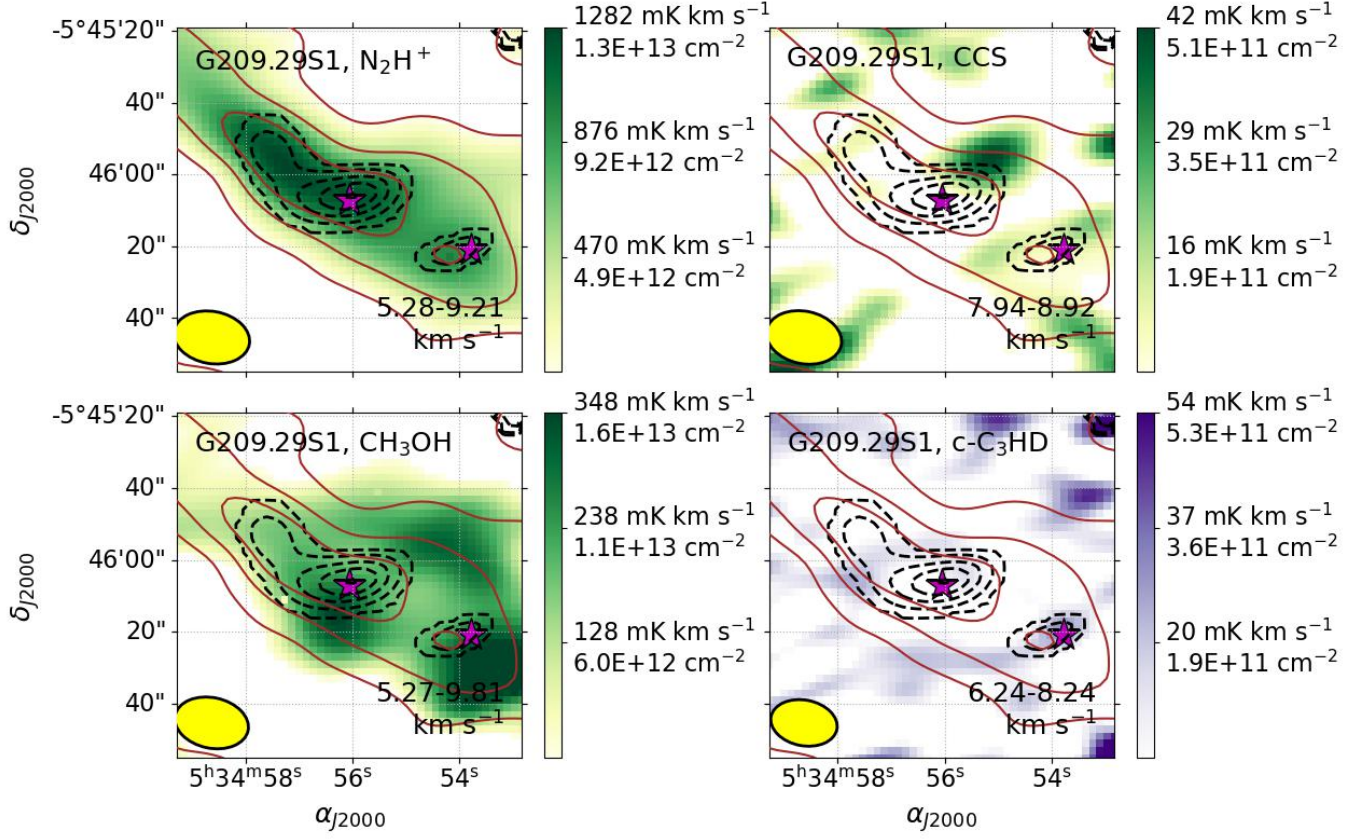


Figure B7. Integrated intensity images of G209.29-19.65S1 (G209.29S1). Please see the context in Appendix B.2 for the captions.

This source, along with another located to the southwest, G209.29-19.65S2 (G209.29S2), is among the targets of this study. The N_2H^+ emission extends slightly to the north. The associated CH_3OH appears to have a feature toward the south, while another localized CH_3OH peak is found at the northwestern boundary of the larger clump. c- C_3HD is not detected near the core. CCS exhibits a core-like feature at the northwest.

B.2.8. G209.29-19.65S2 (G209.29S2)

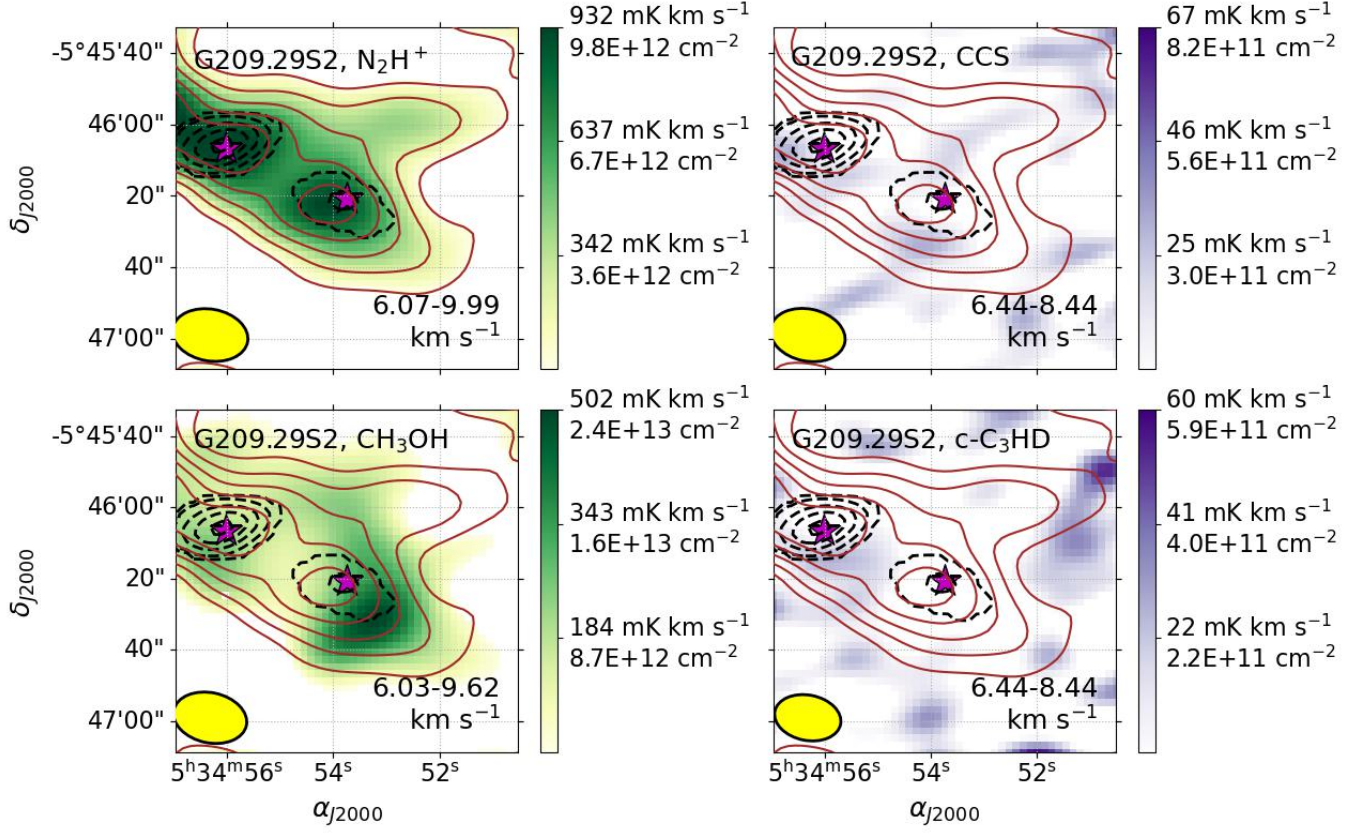


Figure B8. Integrated intensity images of G209.29-19.65S2 (G209.29S2). Please see the context in Appendix B.2 for the captions.

This source, together with G209.29–19.65S1 (G209.29S1) located to the northeast, is one of the targets in this study. Within the extended N_2H^+ structure, the emission peak appears slightly offset from the continuum peak. CH_3OH , in contrast, is distributed toward the southwest of the N_2H^+ peak. Neither c- C_3HD nor CCS is detected in the region neighboring this core.

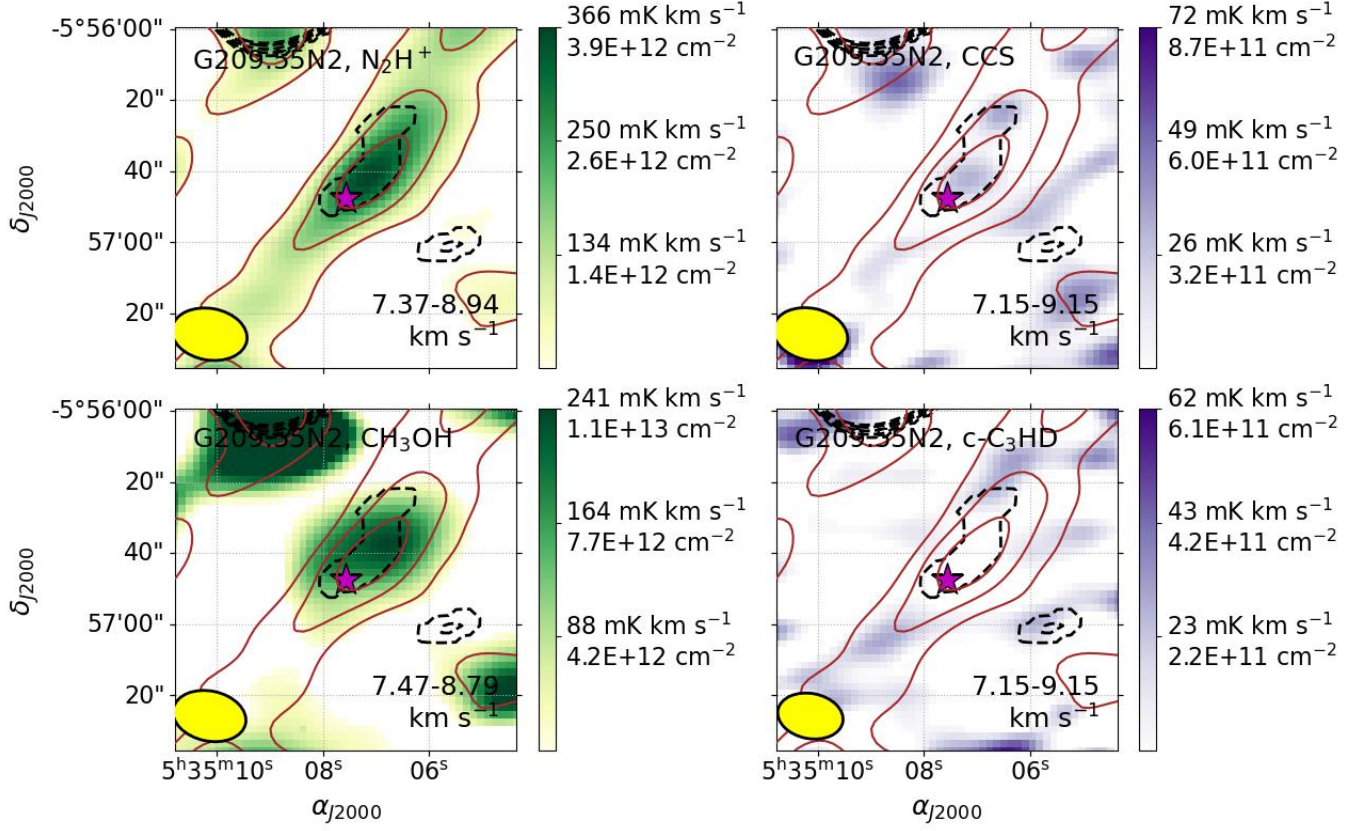
B.2.9. *G209.55-19.68N2 (G209.55N2)*

Figure B9. Integrated intensity images of G209.55-19.68N2 (G209.55N2). Please see the context in Appendix B.2 for the captions.

This source is elongated along the northwest–southeast direction. To the northeast lies the protostellar core HOPS 12 (G209.55–19.68N1 Furlan et al. 2016; Dutta et al. 2020), where a hot corino was detected (Hsu et al. 2022). The color scale of the CH_3OH image is dominated by the emission associated with HOPS 12. It is clear that the CH_3OH emission does not align with the N_2H^+ distribution.

B.2.10. G209.77-19.40E3 (G209.77E3)

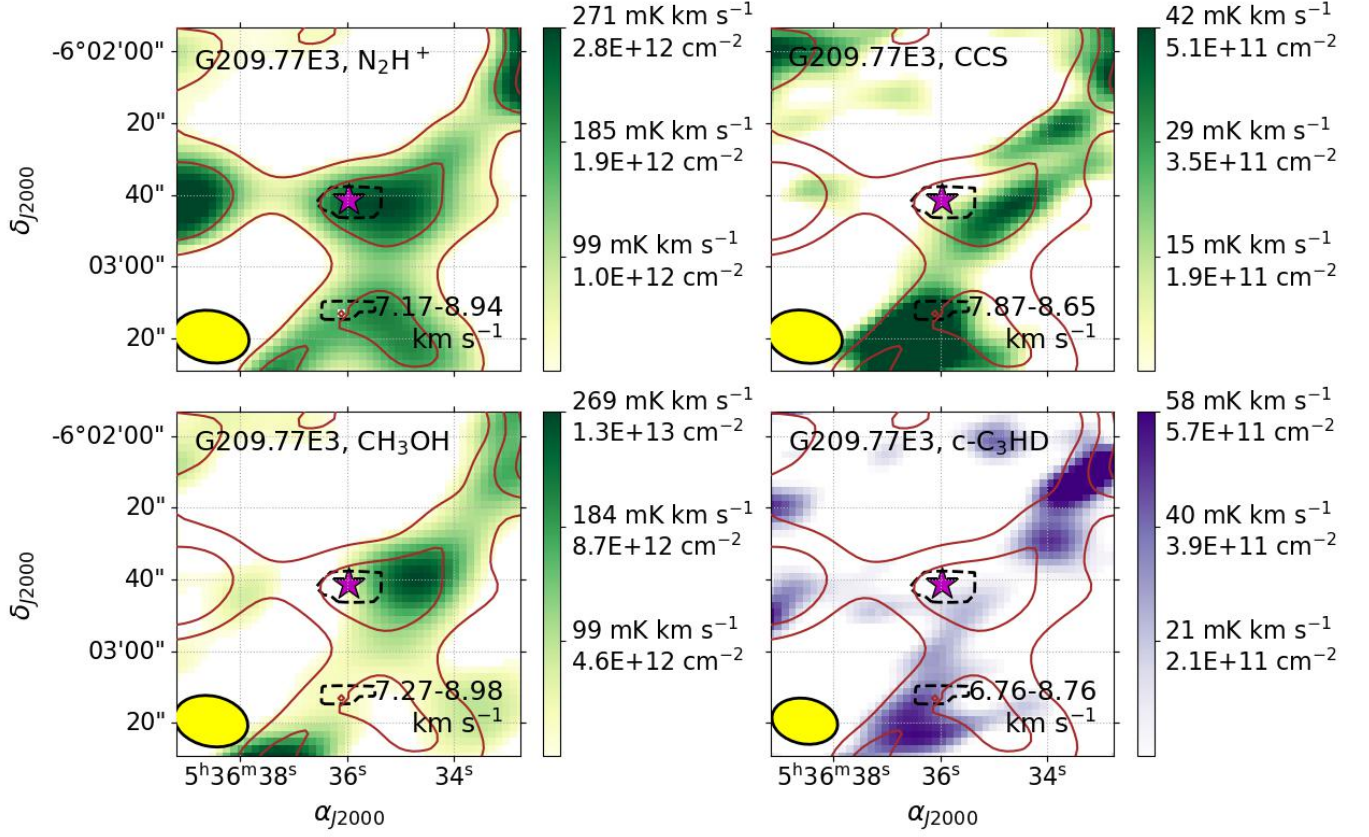


Figure B10. Integrated intensity images of G209.77-19.40E3 (G209.77E3). Please see the context in Appendix B.2 for the captions.

The N₂H⁺ emission from this source is relatively weak, likely due to low gas density. Consistently, the dust continuum is also only weakly detected. The CH₃OH and CCS emissions are distributed toward the northwest and west sides, respectively. c-C₃HD is not detected.

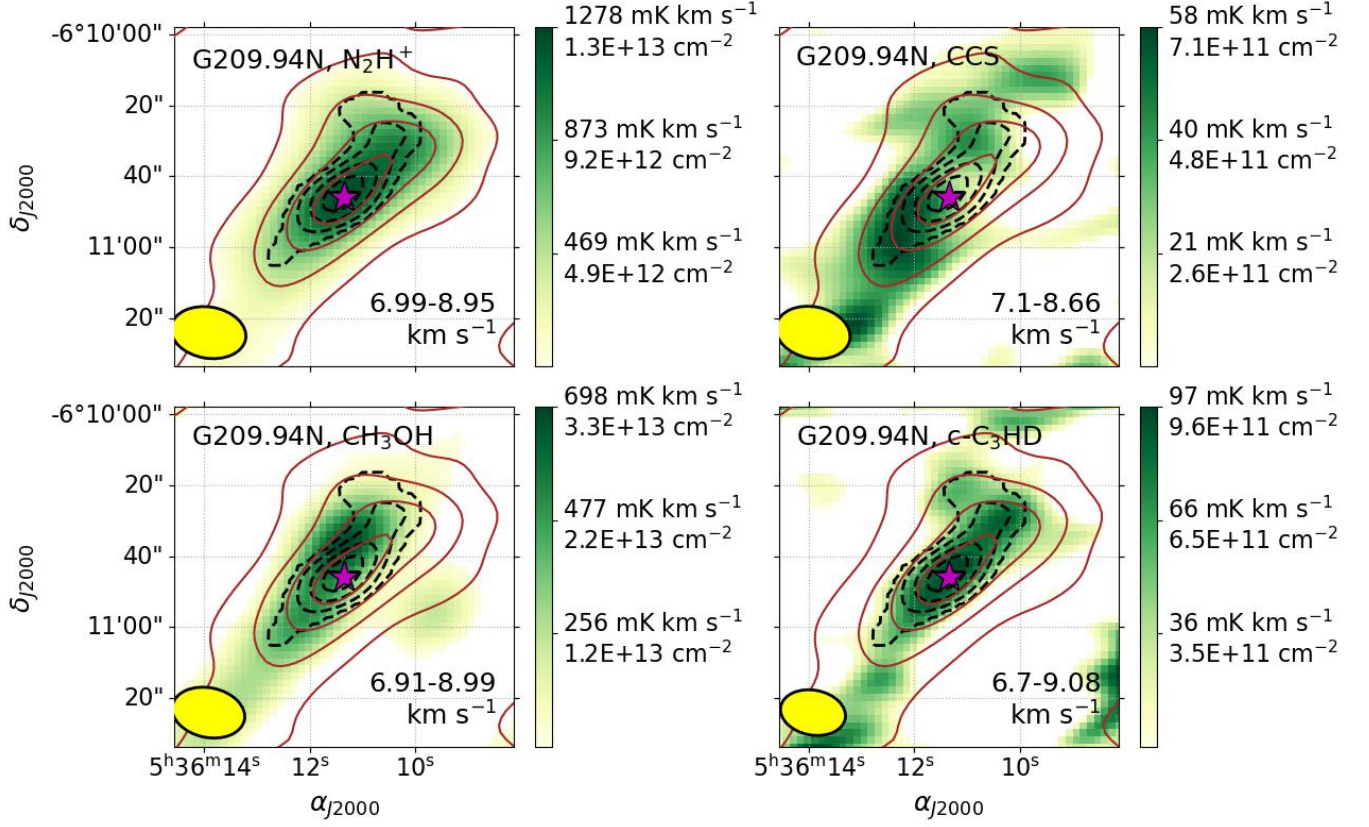
B.2.11. *G209.94-19.52N (G209.94N)*

Figure B11. Integrated intensity images of G209.94-19.52N (G209.94N). Please see the context in Appendix B.2 for the captions.

This clump is elongated in the northwest–southeast direction. N_2H^+ traces the dust continuum beautifully. CH_3OH is distributed on the northeast side of the clump. $c-C_3HD$ is also aligned with the N_2H^+ emission. CCS is present on both the northwestern side and the southeastern corner of the clump, with a peak at the latter location.

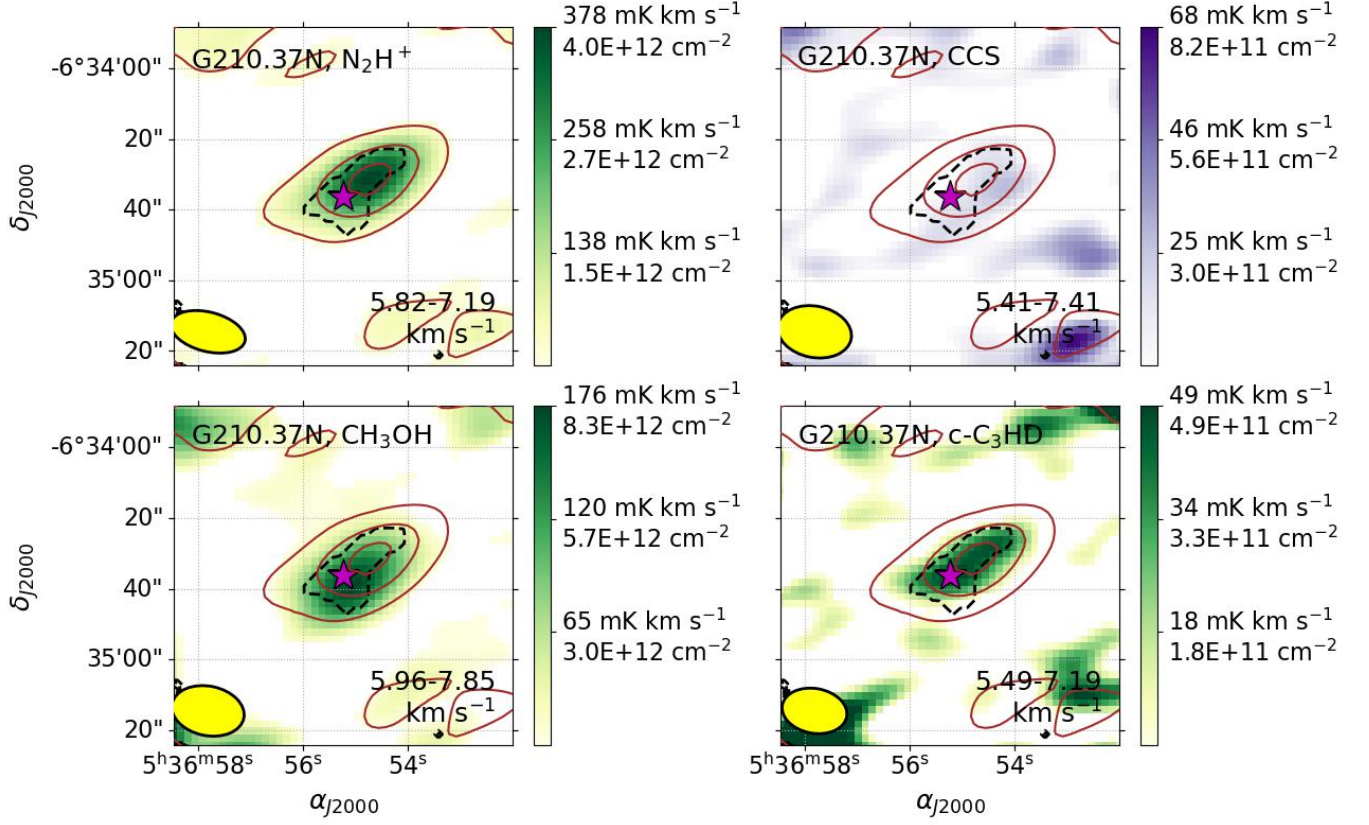
B.2.12. *G210.37-19.53N (G210.37N)*

Figure B12. Integrated intensity images of G210.37-19.53N (G210.37N). Please see the context in Appendix B.2 for the captions.

The continuum and N_2H^+ emissions are slightly elongated in the northwest–southeast direction. CH_3OH is distributed along the southeastern side of the clump. c- C_3HD emission is aligned with the N_2H^+ structure, while CCS is not detected.

B.2.13. G210.82-19.47N2 (G210.82N2)

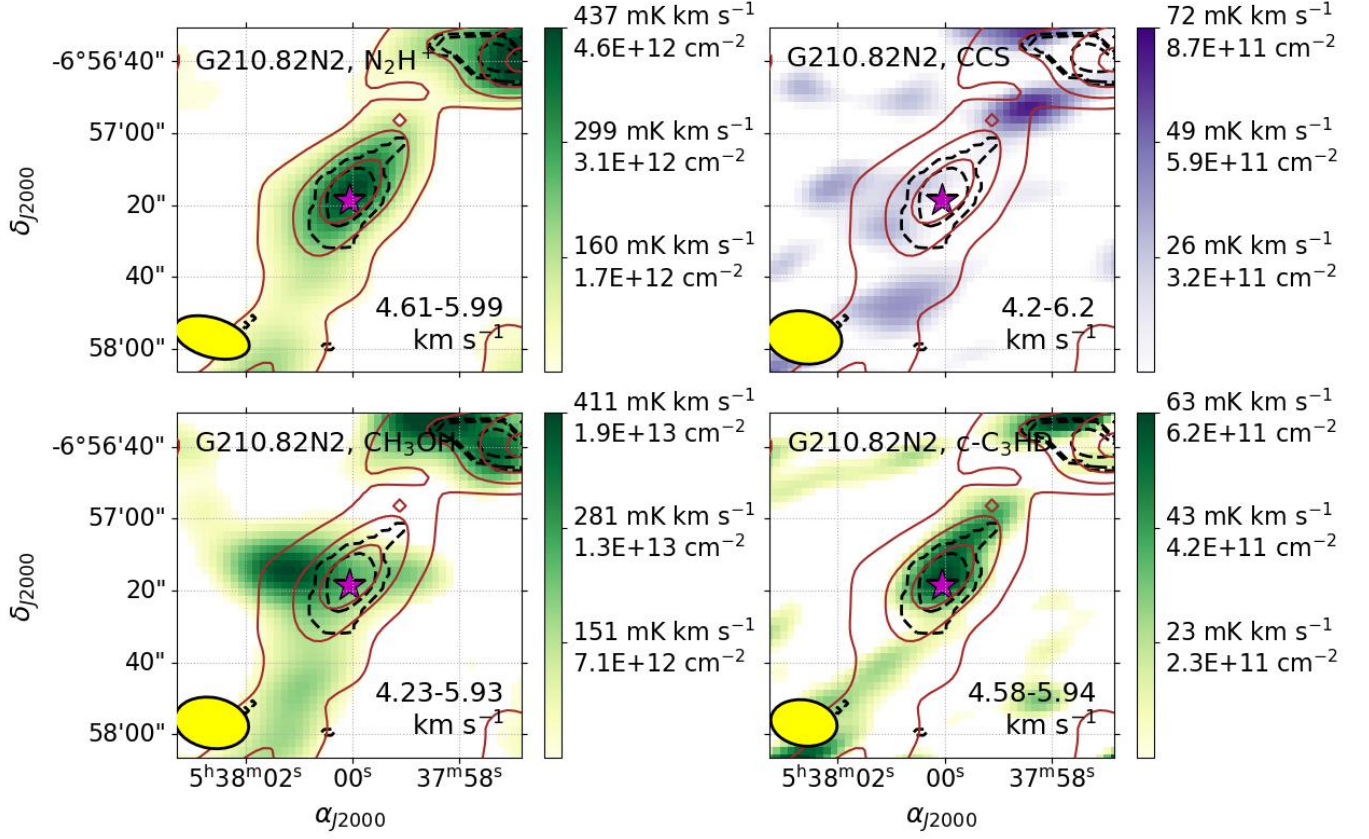


Figure B13. Integrated intensity images of G210.82-19.47N2 (G210.82N2). Please see the context in Appendix B.2 for the captions.

The continuum and N_2H^+ emissions are slightly elongated in the northwest–southeast direction. The CH_3OH emission is peaking at the east side of the clump. c- C_3HD emission is aligned with the N_2H^+ structure, while CCS is not detected. The source at the northwest–southeast side is a protostellar core HOPS 156 (G210.82-19.47N1 [Furlan et al. 2016](#); [Dutta et al. 2020](#)).

B.2.14. G211.16-19.33N4 (G211.16N4)

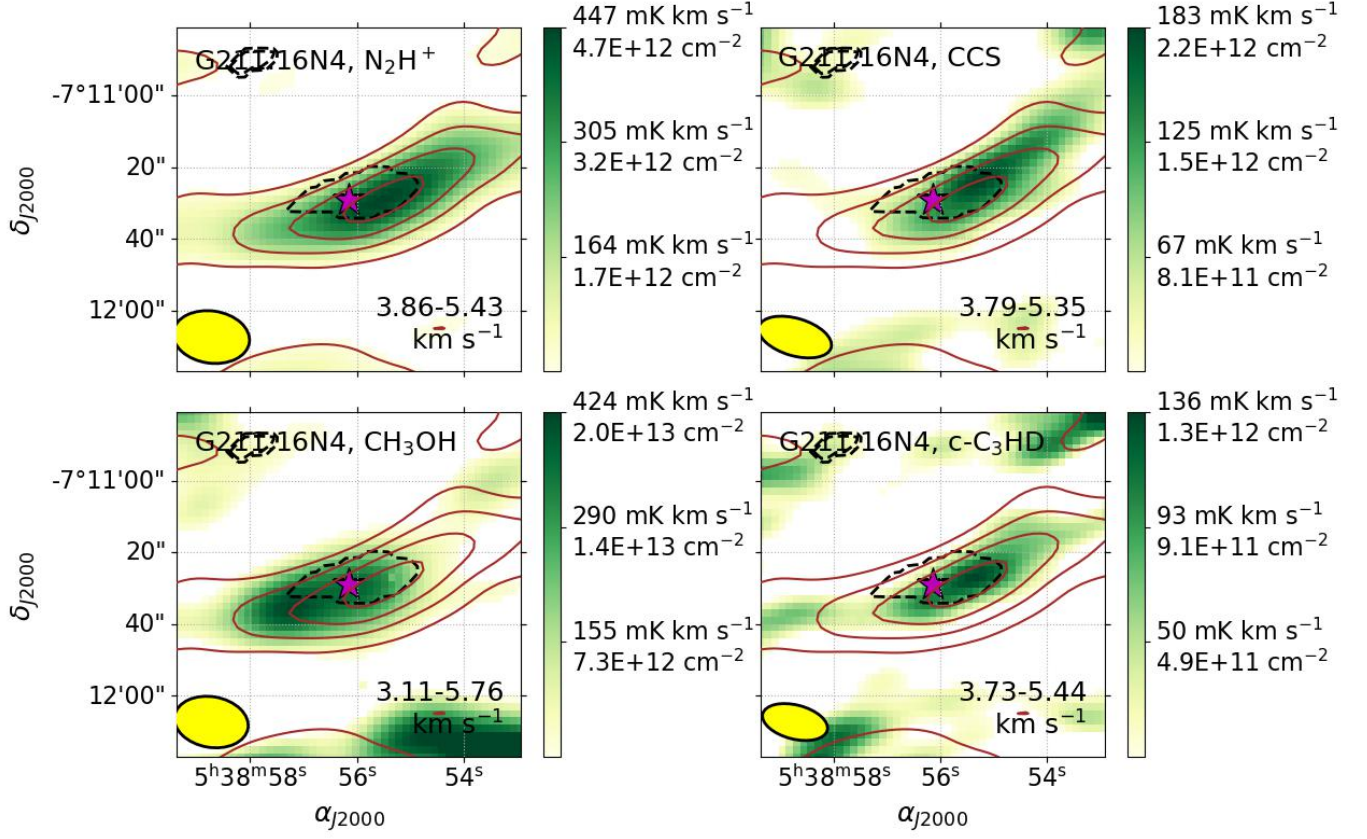


Figure B14. Integrated intensity images of G211.16-19.33N4 (G211.16N4). Please see the context in Appendix B.2 for the captions.

This clump has a filamentary structure oriented in the northwest–southeast direction. The N_2H^+ peak is offset by approximately 10'' to the southwest of the dust continuum peak. Both c-C₃HD and CCS also peak on the southwest side, though their peak positions differ slightly. In contrast, CH₃OH peaks on the southeastern side of the clump.

B.2.15. G211.16-19.33N5 (G211.16N5)

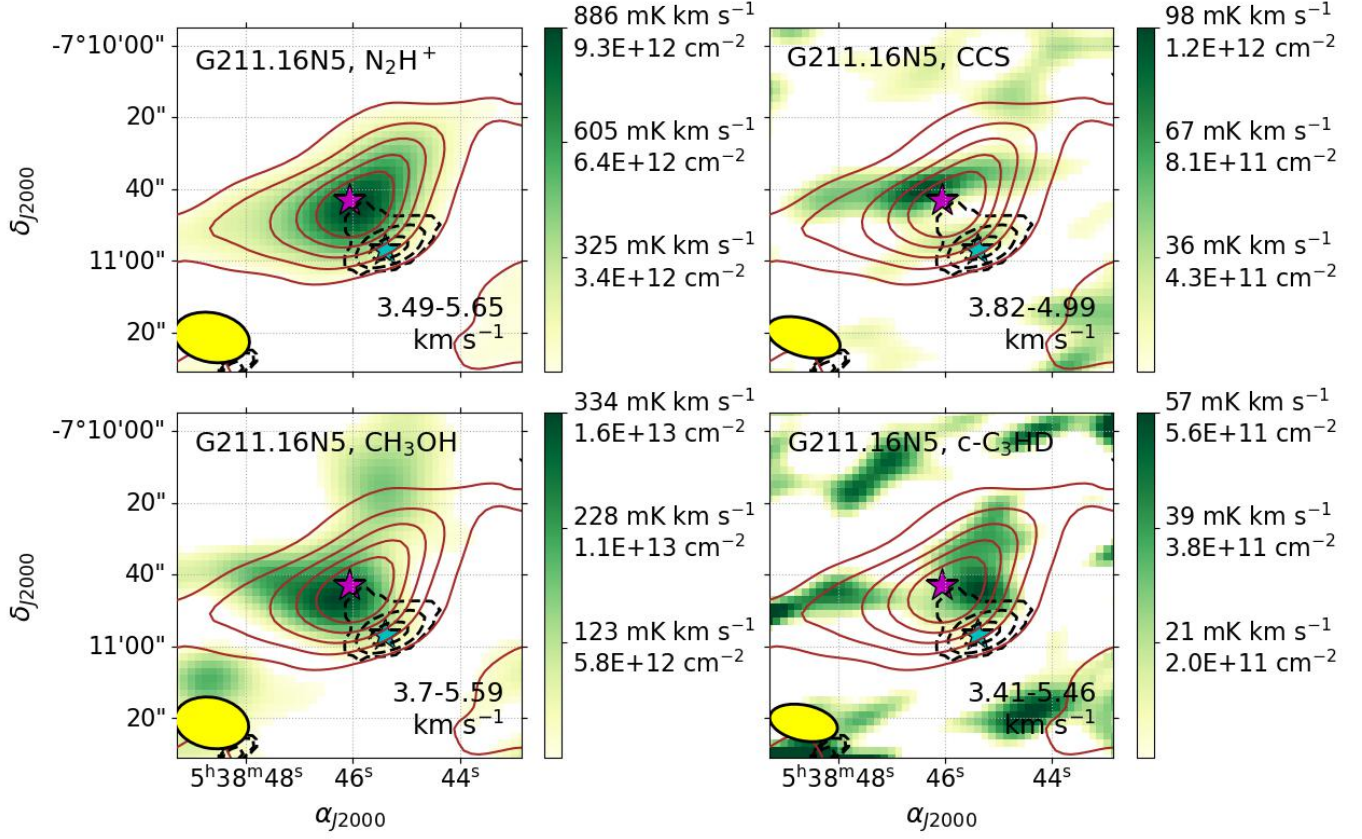


Figure B15. Integrated intensity images of G211.16-19.33N5 (G211.16N5). Please see the context in Appendix B.2 for the captions.

The strong source on the southwest side is the protostellar core HOPS 135 (Furlan et al. 2016). Despite the presence of HOPS 135, it is clear that N_2H^+ is tracing our target, G211.16–19.33N5. CH_3OH appears to have two components on the east and north sides, peaking in the east. Both $\text{c-C}_3\text{HD}$ and CCS are weak, with $\text{c-C}_3\text{HD}$ distributed to the west and CCS to the east.

B.2.16. G212.10-19.15N1 (G212.10N1)

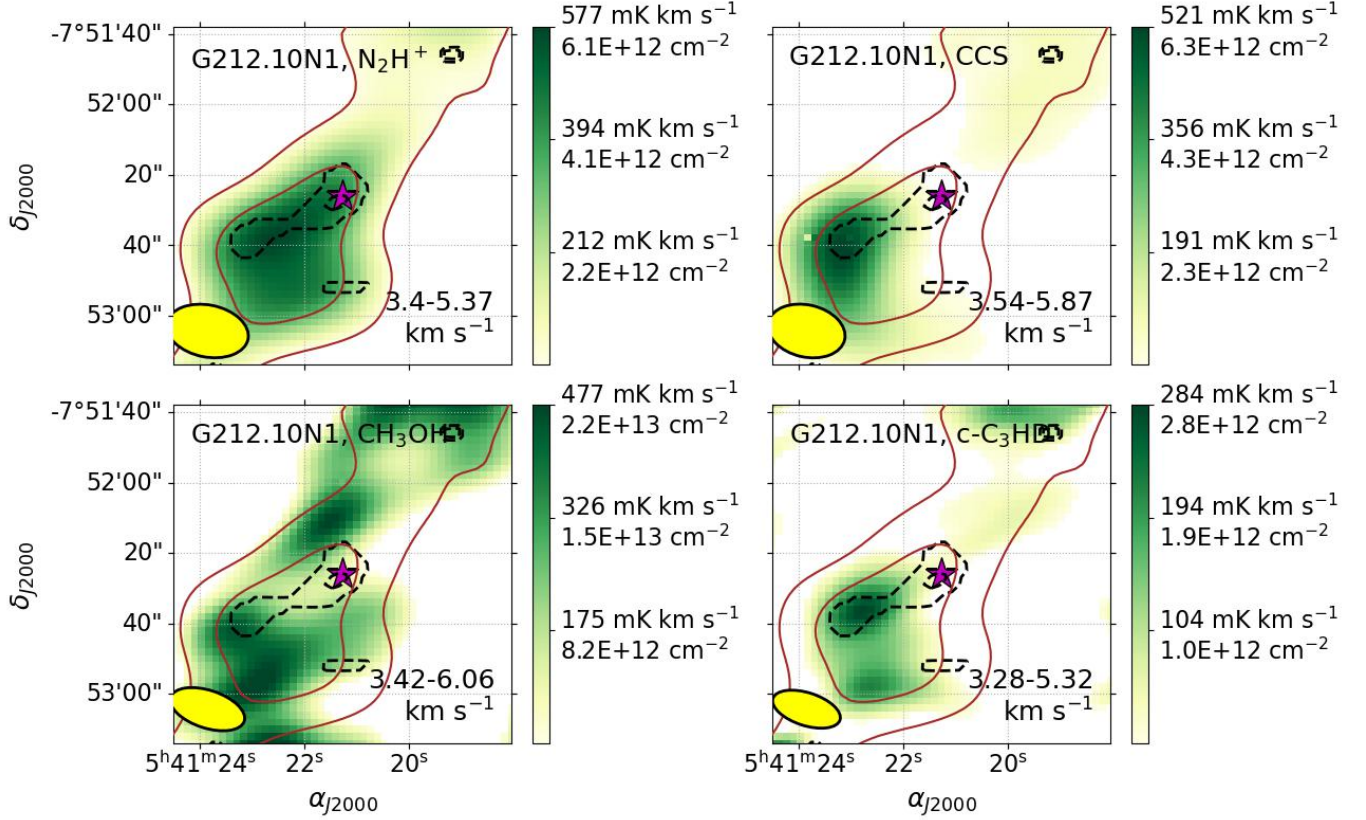


Figure B16. Integrated intensity images of G212.10-19.15N1 (G212.10N1). Please see the context in Appendix B.2 for the captions.

The continuum emission of this clump is fragmented into two substructures, located to the east and west. The N_2H^+ emission exhibits a large diamond-shaped morphology encompassing both continuum components. These two substructures lie on the northeastern side of the N_2H^+ distribution, while the N_2H^+ peak is located between them. CH_3OH is distributed toward the northern and southern corners of the clump. The southern CH_3OH component shows a clear anti-correlation with the N_2H^+ peak. Both $\text{c-C}_3\text{HD}$ and CCS are distributed on the southeastern side of the N_2H^+ structure. The $\text{c-C}_3\text{HD}$ emission appears to split into two features: one lies on the western side of the eastern continuum substructure, and the other on the southern side of the N_2H^+ emission. CCS shows a single component, peaking on the eastern side of the eastern continuum substructure.

REFERENCES

- Arce, H. G., Santiago-Garcia, J., Jorgensen, J. K., Tafalla, M., & Bachiller, R. 2008, *Astrophysical Journal Letters*, 681, L21, doi: [10.1086/590110](https://doi.org/10.1086/590110)
- Astropy Collaboration, Robitaille, T. P., Tollerud, E. J., et al. 2013, *A&A*, 558, A33, doi: [10.1051/0004-6361/201322068](https://doi.org/10.1051/0004-6361/201322068)
- Astropy Collaboration, Price-Whelan, A. M., Sipőcz, B. M., et al. 2018, *AJ*, 156, 123, doi: [10.3847/1538-3881/aabc4f](https://doi.org/10.3847/1538-3881/aabc4f)
- Astropy Collaboration, Price-Whelan, A. M., Lim, P. L., et al. 2022, *ApJ*, 935, 167, doi: [10.3847/1538-4357/ac7c74](https://doi.org/10.3847/1538-4357/ac7c74)
- Bacmann, A., Lefloch, B., Ceccarelli, C., et al. 2002, *A&A*, 389, L6, doi: [10.1051/0004-6361:20020652](https://doi.org/10.1051/0004-6361:20020652)
- Bacmann, A., Taquet, V., Faure, A., Kahane, C., & Ceccarelli, C. 2012, *Astronomy & Astrophysics*, 541, L12, doi: [10.1051/0004-6361/201219207](https://doi.org/10.1051/0004-6361/201219207)
- Balsara, D., Ward-Thompson, D., & Crutcher, R. M. 2001, *Monthly Notices of the Royal Astronomical Society*, 327, 715, doi: [10.1046/j.1365-8711.2001.04787.x](https://doi.org/10.1046/j.1365-8711.2001.04787.x)
- Belloche, A., Maury, A. J., Maret, S., et al. 2020, *A&A*, 635, A198, doi: [10.1051/0004-6361/201937352](https://doi.org/10.1051/0004-6361/201937352)
- Bizzocchi, L., Caselli, P., Spezzano, S., & Leonardo, E. 2014, *A&A*, 569, A27, doi: [10.1051/0004-6361/201423858](https://doi.org/10.1051/0004-6361/201423858)

- Bogey, M., Demuynck, C., Destombes, J. L., & Dubus, H. 1987, *Journal of Molecular Spectroscopy*, 122, 313, doi: [10.1016/0022-2852\(87\)90007-5](https://doi.org/10.1016/0022-2852(87)90007-5)
- Borshcheva, K., Fedoseev, G., Punanova, A. F., et al. 2025, *ApJ*, 990, 163, doi: [10.3847/1538-4357/adea73](https://doi.org/10.3847/1538-4357/adea73)
- Bouvier, M., Ceccarelli, C., López-Sepulcre, A., et al. 2022, *ApJ*, 929, 10, doi: [10.3847/1538-4357/ac5904](https://doi.org/10.3847/1538-4357/ac5904)
- Bouvier, M., Giani, L., Chahine, L., et al. 2025, *MNRAS*, 539, 2380, doi: [10.1093/mnras/staf631](https://doi.org/10.1093/mnras/staf631)
- CASA Team, Bean, B., Bhatnagar, S., et al. 2022, *Publications of the Astronomical Society of the Pacific*, 134, 114501, doi: [10.1088/1538-3873/ac9642](https://doi.org/10.1088/1538-3873/ac9642)
- Ceccarelli, C. 2004, in *Star Formation in the Interstellar Medium: In Honor of David Hollenbach, Chris McKee and Frank Shu*, ASP Conference Proceeding, ed. D. Johnstone, F. Adams, D. Lin, D. Neufeld, & E. Ostriker, Vol. 323, San Francisco, Astronomical Society of the Pacific (ASP Conference Proceedings)
- Chuang, K. J., Fedoseev, G., Qasim, D., et al. 2018, *The Astrophysical Journal*, 853, 102, doi: [10.3847/1538-4357/aaa24e](https://doi.org/10.3847/1538-4357/aaa24e)
- Comrie, A., Wang, K.-S., Hsu, S.-C., et al. 2021, *Astrophysics Source Code Library*, ascl:2103.031, <https://ui.adsabs.harvard.edu/abs/2021ascl.soft03031C>
- Daniel, F., Cernicharo, J., & Dubernet, M. L. 2006, *The Astrophysical Journal*, 648, 461, doi: [10.1086/505738](https://doi.org/10.1086/505738)
- Dartois, E., Chabot, M., Bacmann, A., et al. 2020, *Astronomy and Astrophysics*, 634, A103, doi: [10.1051/0004-6361/201936934](https://doi.org/10.1051/0004-6361/201936934)
- Di Francesco, J., Evans, II, N. J., Caselli, P., et al. 2006, in *Protostars and Planets V*, <https://arxiv.org/abs/astro-ph/0602379>
- Dickens, J. E., Langer, W. D., & Velusamy, T. 2001, *The Astrophysical Journal*, 558, 693, doi: [10.1086/322292](https://doi.org/10.1086/322292)
- Dutta, S., Lee, C.-F., Liu, T., et al. 2020, *ApJS*, 251, 20, doi: [10.3847/1538-4365/abba26](https://doi.org/10.3847/1538-4365/abba26)
- Friberg, P., Madden, S. C., Hjalmarsen, A., & Irvine, W. M. 1988, *Astron Astrophys*, 195, 281, <https://www.ncbi.nlm.nih.gov/pubmed/11540080>
- Furlan, E., Fischer, W. J., Ali, B., et al. 2016, *The Astrophysical Journal Supplement Series*, 224, 5, doi: [10.3847/0067-0049/224/1/5](https://doi.org/10.3847/0067-0049/224/1/5)
- Garrod, R. T., Jin, M., Matis, K. A., et al. 2022, *ApJS*, 259, 1, doi: [10.3847/1538-4365/ac3131](https://doi.org/10.3847/1538-4365/ac3131)
- Garrod, R. T., Wakelam, V., & Herbst, E. 2007, *Astronomy and Astrophysics*, 467, 1103, doi: [10.1051/0004-6361:20066704](https://doi.org/10.1051/0004-6361:20066704)
- Giers, K., Spezzano, S., Lin, Y., et al. 2025, *A&A*, 699, A103, doi: [10.1051/0004-6361/202553843](https://doi.org/10.1051/0004-6361/202553843)
- Giers, K., Spezzano, S., Alves, F., et al. 2022, *Astronomy and Astrophysics*, 664, A119, doi: [10.1051/0004-6361/202243422](https://doi.org/10.1051/0004-6361/202243422)
- Ha, T., Li, Y., Kounkel, M., et al. 2022, *ApJ*, 934, 7, doi: [10.3847/1538-4357/ac76bf](https://doi.org/10.3847/1538-4357/ac76bf)
- Harju, J., Pineda, J. E., Vasyunin, A. I., et al. 2020, *The Astrophysical Journal*, 895, 101, doi: [10.3847/1538-4357/ab8f93](https://doi.org/10.3847/1538-4357/ab8f93)
- Herbst, E., & van Dishoeck, E. F. 2009, *Annual Review of Astronomy and Astrophysics*, Vol 47, 47, 427, doi: [10.1146/annurev-astro-082708-101654](https://doi.org/10.1146/annurev-astro-082708-101654)
- Hirano, N., Sahu, D., Liu, S.-Y., et al. 2024, *The Astrophysical Journal*, 961, 123, doi: [10.3847/1538-4357/ad09e2](https://doi.org/10.3847/1538-4357/ad09e2)
- Hsu, S.-Y., Liu, S.-Y., Liu, T., et al. 2020, *ApJ*, 898, 107, doi: [10.3847/1538-4357/ab9f3a](https://doi.org/10.3847/1538-4357/ab9f3a)
- , 2022, *ApJ*, 927, 218, doi: [10.3847/1538-4357/ac49e0](https://doi.org/10.3847/1538-4357/ac49e0)
- Hsu, S.-Y., Liu, S.-Y., Johnstone, D., et al. 2023, *The Astrophysical Journal*, 956, 120, doi: [10.3847/1538-4357/acefcf](https://doi.org/10.3847/1538-4357/acefcf)
- Hsu, S.-Y., Lee, C.-F., Liu, S.-Y., et al. 2024, *The Astrophysical Journal*, 976, 29, doi: [10.3847/1538-4357/ad7e25](https://doi.org/10.3847/1538-4357/ad7e25)
- Hsu, S.-Y., Liu, S.-Y., Liu, X., et al. 2025a, *ApJL*, 984, L58, doi: [10.3847/2041-8213/adcd6a](https://doi.org/10.3847/2041-8213/adcd6a)
- Hsu, S.-Y., Lee, C.-F., Johnstone, D., et al. 2025b, *ApJ*, 989, 56, doi: [10.3847/1538-4357/ade7fc](https://doi.org/10.3847/1538-4357/ade7fc)
- Jiménez-Serra, I., Vasyunin, A. I., Spezzano, S., et al. 2021, *The Astrophysical Journal*, 917, 44, doi: [10.3847/1538-4357/ac024c](https://doi.org/10.3847/1538-4357/ac024c)
- Jiménez-Serra, I., Vasyunin, A. I., Caselli, P., et al. 2016, *The Astrophysical Journal*, 830, L6, doi: [10.3847/2041-8205/830/1/L6](https://doi.org/10.3847/2041-8205/830/1/L6)
- Jin, M., & Garrod, R. T. 2020, *ApJS*, 249, 26, doi: [10.3847/1538-4365/ab9ec8](https://doi.org/10.3847/1538-4365/ab9ec8)
- Kalvāns, J., & Silsbee, K. 2022, *Monthly Notices of the Royal Astronomical Society*, 515, 785, doi: [10.1093/mnras/stac1792](https://doi.org/10.1093/mnras/stac1792)
- Keown, J., Di Francesco, J., Kirk, H., et al. 2017, *The Astrophysical Journal*, 850, 3, doi: [10.3847/1538-4357/aa93ec](https://doi.org/10.3847/1538-4357/aa93ec)
- Kim, G., Tatematsu, K., Liu, T., et al. 2020, *The Astrophysical Journal Supplement Series*, 249, 33, doi: [10.3847/1538-4365/aba746](https://doi.org/10.3847/1538-4365/aba746)
- Kirk, H., Di Francesco, J., Johnstone, D., et al. 2016, *The Astrophysical Journal*, 817, 167, doi: [10.3847/0004-637X/817/2/167](https://doi.org/10.3847/0004-637X/817/2/167)
- Kounkel, M., Covey, K., Suarez, G., et al. 2018, *Astronomical Journal*, 156, 84, doi: [10.3847/1538-3881/aad1f1](https://doi.org/10.3847/1538-3881/aad1f1)
- Kupilas, M. M., Wareing, C. J., Pittard, J. M., & Falle, S. A. E. G. 2021, *Monthly Notices of the Royal Astronomical Society*, 501, 3137, doi: [10.1093/mnras/staa3889](https://doi.org/10.1093/mnras/staa3889)
- Lin, S.-J., Liu, S.-Y., Sahu, D., et al. 2025, *arXiv e-prints*, arXiv:2509.21158, doi: [10.48550/arXiv.2509.21158](https://doi.org/10.48550/arXiv.2509.21158)
- Lin, Y., Spezzano, S., Sipilä, O., Vasyunin, A., & Caselli, P. 2022, *Astronomy and Astrophysics*, 665, A131, doi: [10.1051/0004-6361/202243657](https://doi.org/10.1051/0004-6361/202243657)
- Lombardi, M., Alves, J., & Lada, C. J. 2011, *A&A*, 535, A16, doi: [10.1051/0004-6361/201116915](https://doi.org/10.1051/0004-6361/201116915)
- Lombardi, M., Lada, C. J., & Alves, J. 2010, *Astronomy and Astrophysics*, 512, A67, doi: [10.1051/0004-6361/200912670](https://doi.org/10.1051/0004-6361/200912670)

- Matthews, H. E., Friberg, P., & Irvine, W. M. 1985, *The Astrophysical Journal*, 290, 609, doi: [10.1086/163018](https://doi.org/10.1086/163018)
- McMullin, J. P., Waters, B., Schiebel, D., Young, W., & Golap, K. 2007, in *Astronomical Data Analysis Software and Systems XVI*, ed. R. A. Shaw, F. Hill, & D. J. Bell, Vol. 376, San Francisco, Astronomical Society of the Pacific (ASP Conference Series)
- Megías, A., Jiménez-Serra, I., Martín-Pintado, J., et al. 2023, *MNRAS*, 519, 1601, doi: [10.1093/mnras/stac3449](https://doi.org/10.1093/mnras/stac3449)
- Nagy, Z., Spezzano, S., Caselli, P., et al. 2019, *A&A*, 630, A136, doi: [10.1051/0004-6361/201935568](https://doi.org/10.1051/0004-6361/201935568)
- Nakai, Y., Sameera, W. M. C., Furuya, K., et al. 2023, *The Astrophysical Journal*, 953, 162, doi: [10.3847/1538-4357/accf95](https://doi.org/10.3847/1538-4357/accf95)
- Ohashi, S., Sanhueza, P., Sakai, N., et al. 2018, *The Astrophysical Journal*, 856, 147, doi: [10.3847/1538-4357/aab3d0](https://doi.org/10.3847/1538-4357/aab3d0)
- Ohashi, S., Tatematsu, K., Sanhueza, P., et al. 2016, *Monthly Notices of the Royal Astronomical Society*, 459, 4130, doi: [10.1093/mnras/stw856](https://doi.org/10.1093/mnras/stw856)
- Okoda, Y., Oya, Y., Imai, M., et al. 2022, *The Astrophysical Journal*, 935, 136, doi: [10.3847/1538-4357/ac7ff4](https://doi.org/10.3847/1538-4357/ac7ff4)
- Oya, Y., Sakai, N., Lopez-Sepulcre, A., et al. 2016, *Astrophysical Journal*, 824, 88, doi: [10.3847/0004-637x/824/2/88](https://doi.org/10.3847/0004-637x/824/2/88)
- Pagani, L., Daniel, F., & Dubernet, M. L. 2009, *A&A*, 494, 719, doi: [10.1051/0004-6361:200810570](https://doi.org/10.1051/0004-6361:200810570)
- Pety, J. 2005, in *SF2A-2005: Semaine de l’Astrophysique Française*, ed. F. Casoli, T. Contini, J. M. Hameury, & L. Pagani, 721
- Planck, C., Ade, P. A. R., Aghanim, N., et al. 2016, *Astronomy and Astrophysics*, 594, A28, doi: [10.1051/0004-6361/201525819](https://doi.org/10.1051/0004-6361/201525819)
- Priestley, F. D., Clark, P. C., Ragan, S. E., et al. 2025, *MNRAS*, 537, 2453, doi: [10.1093/mnras/staf191](https://doi.org/10.1093/mnras/staf191)
- Roberts, J. F., Rawlings, J. M. C., Viti, S., & Williams, D. A. 2007, *MNRAS*, 382, 733, doi: [10.1111/j.1365-2966.2007.12402.x](https://doi.org/10.1111/j.1365-2966.2007.12402.x)
- Rodgers, S. D., & Charnley, S. B. 2001, *The Astrophysical Journal*, 553, 613, doi: [10.1086/320987](https://doi.org/10.1086/320987)
- Sahu, D., Liu, S.-Y., Liu, T., et al. 2021, *The Astrophysical Journal*, 907, L15, doi: [10.3847/2041-8213/abd3aa](https://doi.org/10.3847/2041-8213/abd3aa)
- Sahu, D., Liu, S.-Y., Johnstone, D., et al. 2023, *The Astrophysical Journal*, 945, 156, doi: [10.3847/1538-4357/acbc26](https://doi.org/10.3847/1538-4357/acbc26)
- Sakai, N., & Yamamoto, S. 2013, *Chemical Reviews*, 113, 8981, doi: [10.1021/cr4001308](https://doi.org/10.1021/cr4001308)
- Schöier, F. L., van der Tak, F. F. S., van Dishoeck, E. F., & Black, J. H. 2005, *A&A*, 432, 369, doi: [10.1051/0004-6361:20041729](https://doi.org/10.1051/0004-6361:20041729)
- Scibelli, S., Drozdovskaya, M. N., Caselli, P., et al. 2025, *arXiv e-prints*, arXiv:2508.04762, doi: [10.48550/arXiv.2508.04762](https://doi.org/10.48550/arXiv.2508.04762)
- Scibelli, S., & Shirley, Y. 2020, *The Astrophysical Journal*, 891, 73, doi: [10.3847/1538-4357/ab7375](https://doi.org/10.3847/1538-4357/ab7375)
- Scibelli, S., Shirley, Y., Megías, A., & Jiménez-Serra, I. 2024, *arXiv e-prints*, arXiv:2408.11613, doi: [10.48550/arXiv.2408.11613](https://doi.org/10.48550/arXiv.2408.11613)
- Scibelli, S., Shirley, Y., Vasyunin, A., & Launhardt, R. 2021, *Monthly Notices of the Royal Astronomical Society*, 504, 5754, doi: [10.1093/mnras/stab1151](https://doi.org/10.1093/mnras/stab1151)
- Seo, Y. M., Shirley, Y. L., Goldsmith, P., et al. 2015, *ApJ*, 805, 185, doi: [10.1088/0004-637X/805/2/185](https://doi.org/10.1088/0004-637X/805/2/185)
- Soma, T., Sakai, N., Watanabe, Y., & Yamamoto, S. 2015, *The Astrophysical Journal*, 802, 74, doi: [10.1088/0004-637x/802/2/74](https://doi.org/10.1088/0004-637x/802/2/74)
- Soma, T., Sakai, N., Watanabe, Y., & Yamamoto, S. 2018, *ApJ*, 854, 116, doi: [10.3847/1538-4357/aaa70c](https://doi.org/10.3847/1538-4357/aaa70c)
- Spezzano, S., Bizzocchi, L., Caselli, P., Harju, J., & Brünken, S. 2016, *Astronomy and Astrophysics*, 592, L11, doi: [10.1051/0004-6361/201628652](https://doi.org/10.1051/0004-6361/201628652)
- Spezzano, S., Caselli, P., Bizzocchi, L., Giuliano, B. M., & Lattanzi, V. 2017, *Astronomy and Astrophysics*, 606, A82, doi: [10.1051/0004-6361/201731262](https://doi.org/10.1051/0004-6361/201731262)
- Spezzano, S., Caselli, P., Pineda, J. E., et al. 2020, *Astronomy and Astrophysics*, 643, A60, doi: [10.1051/0004-6361/201936598](https://doi.org/10.1051/0004-6361/201936598)
- Spezzano, S., Redaelli, E., Caselli, P., et al. 2025, *A&A*, 694, A27, doi: [10.1051/0004-6361/202452625](https://doi.org/10.1051/0004-6361/202452625)
- Tafalla, M., Santiago-García, J., Myers, P. C., et al. 2006, *A&A*, 455, 577, doi: [10.1051/0004-6361:20065311](https://doi.org/10.1051/0004-6361:20065311)
- Taillard, A., Wakelam, V., Gratier, P., et al. 2023, *Astronomy and Astrophysics*, 670, A141, doi: [10.1051/0004-6361/202245157](https://doi.org/10.1051/0004-6361/202245157)
- Taniguchi, K., Gorai, P., & Tan, J. C. 2024, *Astrophysics and Space Science*, 369, 34, doi: [10.1007/s10509-024-04292-9](https://doi.org/10.1007/s10509-024-04292-9)
- Tatematsu, K., Kim, G., Liu, T., et al. 2021, *The Astrophysical Journal Supplement Series*, 256, 25, doi: [10.3847/1538-4365/ac0978](https://doi.org/10.3847/1538-4365/ac0978)
- Tatematsu, K., Yeh, Y.-T., Hirano, N., et al. 2022, *ApJ*, 931, 33, doi: [10.3847/1538-4357/ac6100](https://doi.org/10.3847/1538-4357/ac6100)
- Tercero, F., López-Pérez, J. A., Gallego, J. D., et al. 2021, *A&A*, 645, A37, doi: [10.1051/0004-6361/202038701](https://doi.org/10.1051/0004-6361/202038701)
- van Gelder, M. L., Tabone, B., Tychoniec, L., et al. 2020, *A&A*, 639, A87, doi: [10.1051/0004-6361/202037758](https://doi.org/10.1051/0004-6361/202037758)
- Vastel, C., Ceccarelli, C., Lefloch, B., & Bachiller, R. 2014, *The Astrophysical Journal*, 795, L2, doi: [10.1088/2041-8205/795/1/L2](https://doi.org/10.1088/2041-8205/795/1/L2)
- Vasyunin, A. I., Caselli, P., Dulieu, F., & Jiménez-Serra, I. 2017, *The Astrophysical Journal*, 842, 33, doi: [10.3847/1538-4357/aa72ec](https://doi.org/10.3847/1538-4357/aa72ec)
- Vasyunin, A. I., & Herbst, E. 2013, *The Astrophysical Journal*, 769, 34, doi: [10.1088/0004-637X/769/1/34](https://doi.org/10.1088/0004-637X/769/1/34)
- Velusamy, T., Langer, W. D., & Goldsmith, P. F. 2002, *The Astrophysical Journal*, 565, L43, doi: [10.1086/339246](https://doi.org/10.1086/339246)
- Wakelam, V., Dartois, E., Chabot, M., et al. 2021, *Astronomy and Astrophysics*, 652, A63, doi: [10.1051/0004-6361/202039855](https://doi.org/10.1051/0004-6361/202039855)
- Wakelam, V., Gratier, P., Loison, J. C., et al. 2024, *Astronomy and Astrophysics*, 689, A63, doi: [10.1051/0004-6361/202450606](https://doi.org/10.1051/0004-6361/202450606)

- Wakelam, V., Herbst, E., Loison, J. C., et al. 2012, The Astrophysical Journal Supplement Series, 199, 21, doi: [10.1088/0067-0049/199/1/21](https://doi.org/10.1088/0067-0049/199/1/21)
- Xia, J., Tang, N., Zhi, Q., et al. 2022, Research in Astronomy and Astrophysics, 22, 085017, doi: [10.1088/1674-4527/ac784e](https://doi.org/10.1088/1674-4527/ac784e)
- Xu, L.-H., & Lovas, F. J. 1997, Journal of Physical and Chemical Reference Data, 26, 17, doi: [10.1063/1.556005](https://doi.org/10.1063/1.556005)
- Yamamoto, S., Saito, S., Kawaguchi, K., et al. 1990, ApJ, 361, 318, doi: [10.1086/169197](https://doi.org/10.1086/169197)
- Yang, Y.-L., Sakai, N., Zhang, Y., et al. 2021, ApJ, 910, 20, doi: [10.3847/1538-4357/abdfd6](https://doi.org/10.3847/1538-4357/abdfd6)
- Yi, H.-W., Lee, J.-E., Kim, K.-T., et al. 2021, The Astrophysical Journal Supplement Series, 254, 14, doi: [10.3847/1538-4365/abec4a](https://doi.org/10.3847/1538-4365/abec4a)
- Yi, H.-W., Lee, J.-E., Liu, T., et al. 2018, ApJS, 236, 51, doi: [10.3847/1538-4365/aac2e0](https://doi.org/10.3847/1538-4365/aac2e0)
- Zucker, C., Schlafly, E. F., Speagle, J. S., et al. 2018, ApJ, 869, 83, doi: [10.3847/1538-4357/aae97c](https://doi.org/10.3847/1538-4357/aae97c)